Theory and simulation of interactive membrane-macromolecule structures in biological systems

by

Yu-Cheng Su

A thesis
presented to the University of Waterloo
in fulfillment of the
thesis requirement for the degree of
Doctor of Philosophy
in
Physics

Waterloo, Ontario, Canada, 2014

AUTHOR'S DECLARATION

I hereby declare that I am the sole author of this thesis. This is a true copy of the thesis, including any required final revisions, as accepted by my examiners.

I understand that my thesis may be made electronically available to the public.

Abstract

This thesis focuses on one of the branches of soft matter: biological systems. More specifically, we study the morphological transformation of lipid bilayer membranes induced by interacting with macromolecules. Recent progress of the topic is reviewed, and there are two types of systems studied in the thesis; macromolecules can either passively or actively interact with membranes. In the first part, the Monte Carlo simulation is used to study the structural properties of the system consisting of a self-avoiding polymer chain confined between a fluid membrane and a flat hard surface. There are no attraction or repulsion between the polymer and the membrane, and the membrane is adhesive to the flat surface or is pressed against the surface due to a pressure difference. As the adhesion between the soft membrane and the surface increases, the polymer is subject to a strong confinement; the state containing a pancake-shaped polymer conformation eventually yields to a bud state through an abrupt, discontinuous structural transition. We explore the scaling behavior of the physical properties of the system as functions of the polymer's size, the membrane's surface tension, and the adhesion energy. As for the pressure difference case, we show that it has a discontinuous structural phase transition. Monte Carlo simulations reveal that the system undergoes a transition from a confined (bump) state to a strongly confined (flatten-out) state as the pressure increases. A scaling argument is also made to understand the physical mechanism behind the phase transition and the properties of each state. In the second part, to understand how the nanoparticle adhesion strength and the deformation capability induce different protruding membrane structures, a model based on grand canonical ensemble and its solution are presented. With free energy minimization, we demonstrate that multiple nanoparticles with certain range of the adhesion strength and the deformation capability are able to induce stably not only tubes and buds but also pearls, and the structure diagrams of these shapes were computed. The results suggest that the pearling structure results from a balance between the adhesion strength, the deformation capability and the reduced volume of the vesicle. We also find a structural transformation that a tubular structure changes abruptly into a pearling structure.

Acknowledgements

In so many ways I have been enjoying the Ph.D. process, and for this, I am indebted to so many people for their support, encouragement, and friendship. I am grateful to Professor Jeff Z. Y. Chen for his guidance throughout my Ph.D. program. I am also grateful to Professors Thomas Weikl, Roger Melko, Mikko Karttunen, and Zoya Leonenko for their helpful feedbacks on my work. I would also like to thank Professor Wing-Ki Liu for his kind advice when I first came to Canada, and being the teaching assistant of his class was quite enjoyable.

The incredible friendship I have is one of the biggest support for me. Wuyang Zhang, Zijiang Long, Ying Jiang, Sergey Mkrtchyan, and Yeongyoon Kim welcomed me warmly when I first came to Waterloo and kindly helped me settle in the place. I am also encouraged a lot by the interesting conversations I have with Yu Chai, Qinrong Zhang, Haipeng Su, Yan Hao, Siyuan Bian, Yao Li, Han Maio, Jie Gao, Siriporn Pansri, Kier von Konigslow, and Qianshi Wei. Their words inspired me constantly. Also, I would like to thank Judy Nicholl. Her positive attitude really encouraged me during the thesis writing process. Special thanks to Jen-Chien Chang, Guo-Yuan Lien, and Tung-Chang Liu for their hospitality when I visited University of Maryland and the long trip they had driving all the way from U.S. to Waterloo to visit me.

Finally, I am thankful to Chia-Ning Chou and my parents. Their endless support and encouragement help me overcome obstacles in my life. I would not have completed my Ph.D. study without their encouragement.

To my family

Table of Contents

List of Figures

Chapter 1

Introduction and overview

1.1 Soft matter—main ingredients

The basic aim of soft condensed matter physics is to study the properties of the collective behaviors of aggregated molecules; the states of the molecules studied by soft matter physicists are neither simple liquids nor crystalline solids. Some of them are familiar from everyday life, such as glues, soaps, and rubbers; Some of them even becomes very important in successful commercial products, such as LCDs (Liquid Crystal Displays) that relies on the optical properties of liquid crystals. Of course, the biological materials we are made of is also soft matter. Many such materials exhibits novel and counter-intuitive phenomena that are quite different from the traditional solid state physics. For example, in the common-sense of thermal expansion, heating an object results in expanding its volume. However, heating a rubber band causes it to contract rather than expand.

To explain this seemingly contradicting behavior, let's model the rubber band as a cross-linked network composed of many polymer chains. Let's simplify the model even further by just considering the behavior of a single polymer chain (Fig. 1.1). We know from statistical mechanics [85] that an equilibrium state is determined by finding the minimum of its free energy F and that increasing the entropy decreases the free energy because

$$F = E - TS, \tag{1.1}$$

where E is the energy of the system. The entropy of a system is determined by the number of possible states it can have. Thus, if the chain is stretched, the number of possible states decreases, and so does the entropy. Conversely, if the chain is unstreched,

Figure 1.1: The structure of rubber bands can be modelled as a cross-linked network formed by polymer chains. The model is further simplified to consider the behavior of a single polymer chain.

the chain possesses higher entropy. Because heating the chain introduces disorder (more possible states) and increases the entropy, the chain is more likely to stay in a unstreched status. Thus, macroscopically, the rubber band contracts when being heated.

The above example provides us some insights of two important features of soft matter:

- *Coarse-grained model.* The length scales of many soft matter systems are between atomic scales and macroscopic scales. It is possible to construct a coarse-grained model without considering every details at atomic scales. This property is crucial for the main theme of this thesis, that is, lipid bilayer membranes. In the rubber band example, instead of considering the detailed atomic units of which the polymer chain is composed, we model the polymer chain as a long, flexible filament in the space.

- *Thermal fluctuations.* Brownian motions induced by the thermal fluctuations plays an important role in soft matter systems. To understand the thermal contraction of rubber bands, the entropy of the polymer chain is taken into account. The size of the typical energies associated with soft matter systems are usually comparable with the size of the thermal energies, and interesting phenomena take place when the energy (E) and the entropy (S) in Eq. (1.1) competes with each other.

We will see these two features recurring throughout the thesis.

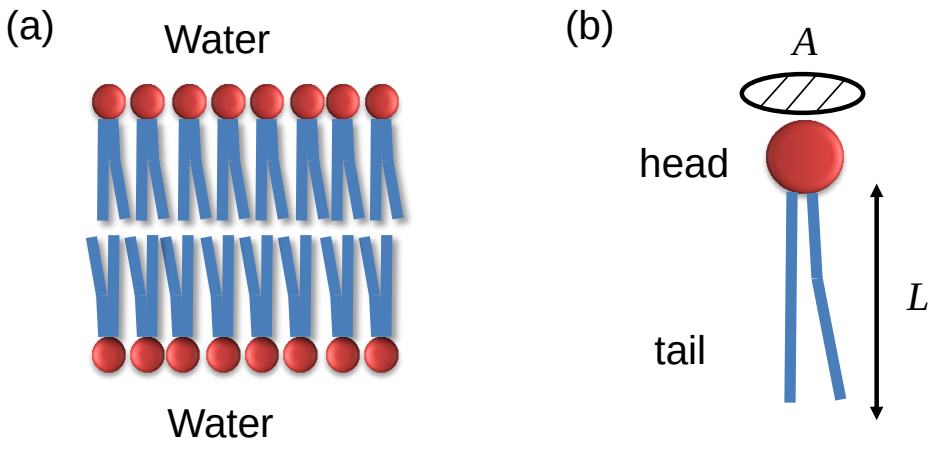

Figure 1.2: (a) The tails (hydrophobic) is shielded by the heads (hydrophilic) to avoid contact with water. (b) A simple depiction of a phospholipid molecule.

1.2 Lipid bilayer membranes

Lipid bilayer membranes are the biological materials that build up the cell and isolate it from the environment [1]. The membranes confine other biological materials and define the cell boundaries. Lipid bilayer membranes are composed of phospholipids, which are amphiphilic molecules that the head of the molecule is hydrophilic (love water) and the tail is hydrophobic (hate water). The lipids self-assemble through Brownian motion in a way that the hydrophobic parts (tail) are hidden from the water, shielded by the hydrophilic parts (head) (Fig. 1.2(a)).

Fig. 1.2(b) shows the structure of a phospholipid, which is similar to a soap molecule. However, one important difference is that the tail of the phospholipid has two hydrocarbon chains, which makes the lipid more like in a cylindrical shape. A simple yet informative geometry argument [59] provides an insight into how this shape prompts phospholipids to aggregate in sheets and stack into bilayers. Assume that a single lipid inside the aggregate takes an area A with a volume V, and its tail length is L. For a bilayer aggregate, formed by N lipids, with a thickness d and membrane area A_{mem}, it has to satisfy the following relations:

$$NA = 2A_{\text{mem}}, \tag{1.2}$$

$$NV = dA_{\text{mem}}. \tag{1.3}$$

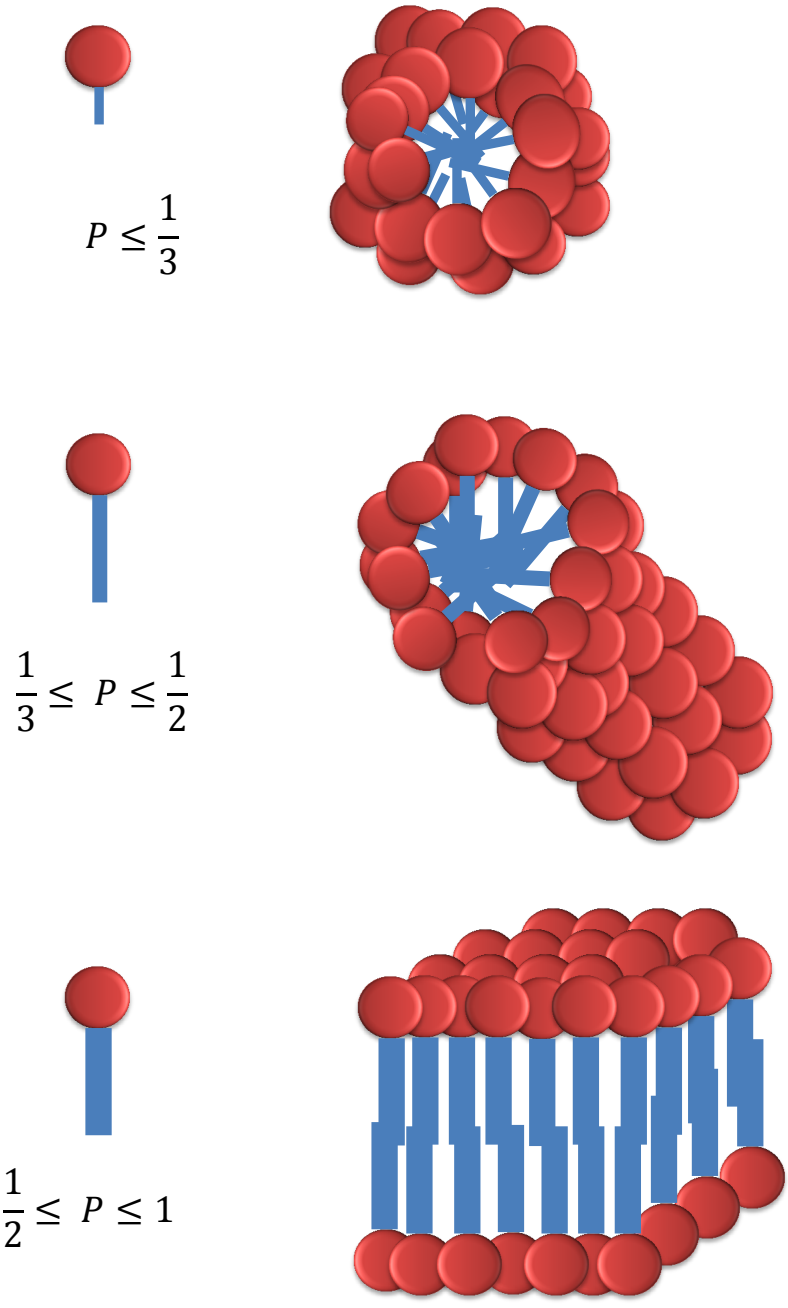

Figure 1.3: A schematic summary about how the packing parameter P shapes the lipid aggregates.

Rearranging the above equations we have $d = 2V/A$. Since we don't want any empty space inside the bilayer, the combined tail length $2L$ must be greater than the thickness d, that is, $2L \geq d$. Expressing the above relations in terms of volume and area, we have

$$P = \frac{V}{AL} \leq 1, \quad \text{for bilayers,} \tag{1.4}$$

where P is referred to as the *packing parameter*. The above argument can also be applied to a spherical or a cylindrical aggregate. The results are

$$P = \frac{V}{AL} \leq \frac{1}{3}, \quad \text{for spherical aggregates,} \tag{1.5}$$

$$P = \frac{V}{AL} \leq \frac{1}{2}, \quad \text{for cylindrical aggregates.} \tag{1.6}$$

The above relations are summarized in Fig. 1.3. A small packing parameter corresponds to molecules with a big head and a short tail, which tend to aggregate into spheres. On the other hand, a larger packing parameter corresponds to a more cylindrical shape, which tend to aggregate into bilayers. Thus, because of having two tails, the phospholipids are able to self-assemble into quasi-two dimensional objects. The argument serves as an good example of coarse-graining. Without going into the detailed atomic structures of phospholipids, we are able to give a reasoning of why lipids tend to aggregate into bilayers.

An important structure formed by lipid bilayer membranes is called *vesicle*. When lipid molecules stack into sheets, an energy cost appears at the edge since the tails at the edge are exposed to water. However, one possible structure that eliminates the edges is to form a closed surface of bilayers. Such a structure is known as a vesicle. Vesicles can be considered to be a simple model of biological cells, separating its content from the environment. They are also important as a tool of encapsulating molecules and delivering them to a target inside the body, which has a potential application of the pharmaceutical industry.

1.3 Modelling membranes

1.3.1 Membranes as thin elastic sheets

When macromolecules adhere to the surface of membranes, it costs energy to bend or to deform the surface. Typically, the thickness of lipid bilayer membranes is $d \sim 5$ nm, and the surface area that spans a vesicle can be $10 \sim 10000\,\mu\text{m}^2$ [8]. This implies that the

dimension of thickness can be neglected, and it is reasonable to regard bilayers as thin elastic sheets. The bending energy needed to deform the surface is modelled by Helfrich energy [20, 55]:

$$E_{\text{bend}} = \frac{\kappa}{2} \int (c_1 + c_2 - c_0)^2 \, dA + \kappa_{\text{G}} \int c_1 c_2 \, dA, \tag{1.7}$$

where c_1 and c_2 are the principal curvatures that describe the curvature of the element area dA. The simple average of c_1 and c_2 is known as the mean curvature $M = (c_1 + c_2)/2$ while the product $c_1 c_2$ is known as the Gaussian curvature [65]. The spontaneous curvature c_0 accounts for any tendency of the membrane to bend in one direction or another. For a single component membrane, the spontaneous curvature must be zero due to the symmetric packing of lipids. On the other hand, the spontaneous curvature is generated when molecules adhere to or are embedded in the membranes, which causes asymmetry between the two layers.

The constant κ is known as the *bending modulus*. A stable membrane has a positive bending modulus. The typical value of κ is around tens of $k_{\text{B}}T$ [8], where k_{B} is the Boltzmann constant and T is the temperature. The bilayer's thermal undulation can be exploited to measure the value of κ in experiments [14, 13, 98, 99, 46, 56] and in computer simulations [49, 70, 5, 44, 74, 114, 29, 28, 10, 113].

The constant κ_{G} is called *saddle-splay modulus*. In contrast to the bending modulus, the value of the saddle-splay modulus is harder to estimate either in experiments or in computer simulations. Recently, a fairly accurate method to determine κ_{G} in computer simulations has been proposed [58]; a MARTINI lipid model [74, 75] representing DMPC membrane was studied and $\kappa_{\text{G}}/\kappa \sim -0.9$ was obtained.

There is one important simplification in Helfrich model, Eq. 1.9, which involves the Gaussian curvature $c_1 c_2$. The Gauss-Bonnet theorem [65] states that the integral of the Gaussian curvature over a closed surface is an constant that depends only on the topology of the surface, not its detailed shape. Specifically, as long as distortions of a closed surface involves no change in topology, we have

$$\int c_1 c_2 \, dA = \textit{constant}. \tag{1.8}$$

Therefore, for deformations without any changes in topology, the bending energy is simply given by

$$E_{\text{bend}} = \frac{\kappa}{2} \int (c_1 + c_2 - c_0)^2 \, dA. \tag{1.9}$$

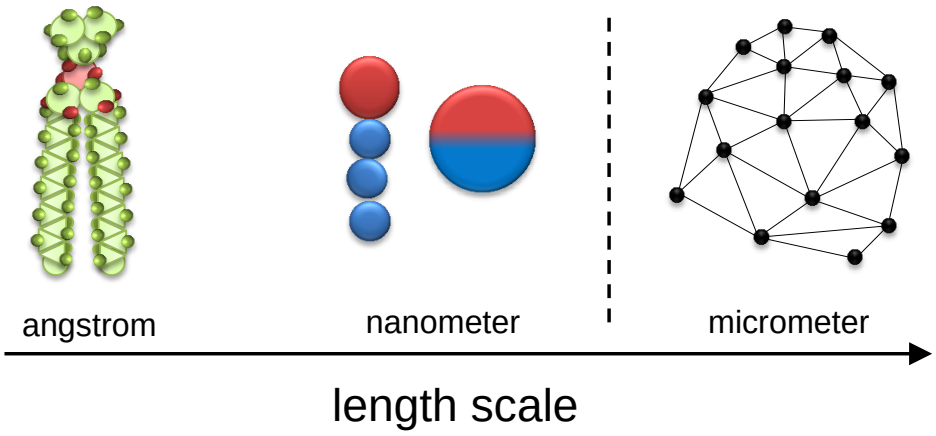

Figure 1.4: Different particle-based models have been proposed to simulate bilayer membranes at different length scales. The first two types of models (from the left side of the figure) simulate lipids in atomic scale or in different levels of coarse-graining. The other type of models construct the membrane surface through a network without any notion of phospholipids.

1.3.2 Membranes in computer simulations

Following the bilayer structures presented in Sect. 1.2, it is natural to model the membrane systems using particle-based models. One that deals with molecular details is the atomistic model. This type of models is able to describe the molecular organization and dynamics of the lipids. A nice review of atomistic models can be found in Ref. [78]. In the following discussion, we highlight some of the coarse-grained models that each lipid molecule is constructed with a certain degree of coarse-graining in the simulation. Depending on modelling phospholipids explicitly or not to represent membranes, they can be classified into two groups, as shown in Fig. 1.4.

The first group models bilayer membranes with coarse-grained phospholipids. Since the formation of lipid bilayers are driven by the aversion of the lipid's hydrophobic part to exposure to water, it is natural to include the water molecules into models [50, 116, 67]. While it is straightforward to include solvent particles into simulations, it increases computational cost a lot, limiting the accessible time and length scales. To overcome the limitation, solvent-free models are developed [83, 44, 114, 29, 28, 11, 92, 90]. However, the parametrization of such models is less intuitive, and some experimentally relevant

membrane properties, such as the size of bending modulus, are hard to control. It is also possible to represent a cluster of phospohlipids by only one particle. The first of such models was proposed by Drouffe *et al.* [41], and along this direction, several models were proposed [9, 7, 63]. The second group models membranes with a network-like structure, purely exploiting the elastic properties of membranes without any notion of phospholipids. The most common representation is the triangulated-network model [51, 39, 82, 2, 69]. This type of models is valid for larger length scales, for example, in micrometer level, but it cannot account for topological changes such as budding.

Besides particle-based models, membrane systems can be modelled as continuous surfaces. The standard approach is writing all the interaction energies in the context of Helfrich model and performs minimization with proper constraints to find the free energy minimum. This approach is relatively fast and computationally inexpensive compared to particle-based models. However, it is difficult to include the effect of thermal fluctuations into models. One common method to minimize free energy is deriving the shape equations from the free energy functional [101, 76]. This type of models has been widely used to study membrane systems with axis symmetry. A nice review on treating membranes as continuous surfaces to explore various membrane properties can be found in Ref. [100].

1.4 Macromolecules interacting with membranes

Generally, there are two ways that macromolecules can interact with membranes to deform and to generate curvature: macromolecules can be either embedded in the lipid bilayer membranes or adsorbed onto the membrane surface. In this discussion, we will focus on the membrane deformation induced by adsorption and also some membrane structures produced purely by excluded-volume interaction.

1.4.1 A simple analysis on one spherical particle problem

Let us start from a simple case. A spherical particle with a radius R_p is adsorbed onto a flat membrane surface. We assume the depth of the adsorption h is much smaller than the radius R_p, and the contact area between the particle and the membrane is $A_\mathrm{cap} = 2\pi R_\mathrm{p} h$. The setup of the system is illustrated in Fig. 1.5. According to Helfrich model, the bending energy in this case is $2\kappa A_\mathrm{cap}/R_\mathrm{p}^2$. Since the originally flat membrane is now deformed and stretched, a cost of surface tension energy has to be taken into account, which is $\sigma\pi h^2$, where σ is the surface tension, and πh^2 is the area difference between the contact area A_cap

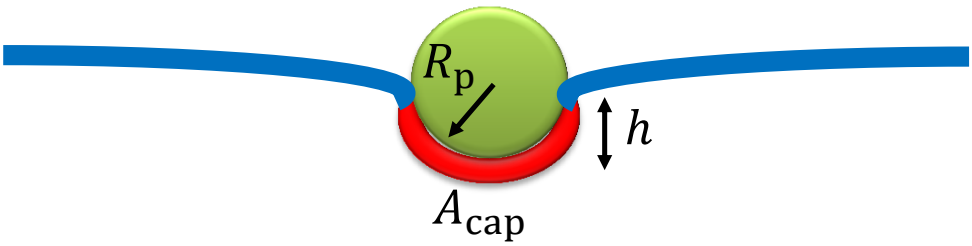

Figure 1.5: An adsorbed spherical particle deforms the membrane surface.

and its projected area to the flat surface. The surface tension energy can be expressed in terms of S_{cap}, that is, $\sigma\pi h^2 = \sigma A_{\text{cap}}^2/(4\pi R_{\text{p}}^2)$. The adhesion energy due to adsorption is $-\epsilon A_{\text{cap}}$, where ϵ is the adhesion constant per unit area. Combining the above three terms, the free energy of the system is

$$F = 2\kappa\frac{A_{\text{cap}}}{R_{\text{p}}^2} + \sigma\frac{A_{\text{cap}}^2}{4\pi R_{\text{p}}^2} - \epsilon A_{\text{cap}}. \tag{1.10}$$

Minimizing the free energy with respect to A_{cap}, we obtain the following expression,

$$\frac{A_{\text{cap}}}{4\pi R_{\text{p}}^2} = \frac{\epsilon - \kappa/R_{\text{p}}^2}{2\sigma}. \tag{1.11}$$

The result suggests that, for a particle to be adsorbed on the membrane, the adhesion has to be strong enough to overcome the cost of bending energy; otherwise, the particle departs from the membrane even if there is adhesion between the particle and the membrane. Moreover, for zero surface tension, the particle becomes wrapped as soon as $\epsilon > 2\kappa/R_{\text{p}}^2$.

1.4.2 One particle problem

The above analysis gives us a general picture of the problem. The one particle adhesion model has been studied extensively because not only it serves as a basic model to understand how membranes are deformed by outsiders but also it resembles a process called *endocytosis*, which cells absorb molecules (such as proteins) by engulfing them. A large body of theoretical works have been conducted to understand the nature of this process

[71, 37, 36, 48, 103, 53, 68, 118, 21]. An early work [71] neglecting the contribution of surface tension predicted that the adsorbed particle can either be unbound or fully wrapped, which does not explain the partial wrapping observed in experiments and simulations. Recent studies [37, 36] using shape equations derived from the free energy functional shows that increasing the adhesion constant ϵ leads to a continuous binding followed by a discontinuous wrapping transition. These findings agree with the results of particle-based simulations [103, 118]. Also, the membrane deformation caused by a single adhesive non-spherical particle have been explored and found results similar to the spherical particle cases [25, 117, 112, 118, 34]. Some experiments have been performed to understand the interaction between a single nanoparticle and a bilayer membrane [61, 93]. Interestingly, Ref. [61] reported that the cell functions altered by nanoparticles depends on the size of nanoparticles.

1.4.3 Many particles problem

When two particles are adsorbed on the membranes, the deformation responds in a way that minimizes the cost of bending energy and maximizes the contact area between nanoparticles and the membrane, which can result in effective interactions between adsorbed particles. These membrane-mediated interaction can be either attractive or repulsive. For example, two cylindrical particles adhering to a planar membrane perturbs the membrane shape. An effective attractive interaction is mediated through the membrane deformation for cylinders adhering to the opposite side of the membrane. On the other hand, an effective repulsive interaction is mediated for cylinders adhering to the same side of the membrane [115, 80, 77]. It has also been shown that, for two adsorbed spherical particles in the strongly curved membrane regime, a crossover from repulsive to attractive pair-interactions emerges [91].

The behaviors of adsorbed nanoparticles become more versatile when there are three or more adhering particles. With particles that have no attractions to each other in the solution, Koltover *et al.* experimentally observed that two nanoparticles bound to a vesicle surface tend to approach each other and bound after a period of time. When a third particle is added into the system, a chain-like triplet was formed instead of an isotropic triangular formation [64]. With multiple nanoparticles different arrangement of nanoparticles can be formed. Theoretical studies have shown that based on the size of nanoparticles [120] and the bending rigidity of a membrane [95], the nanoparticles can self-assemble into hexagonal closed packing or linear aggregates, as shown in Fig. 1.6. For large deformation, it has been shown in computer simulations that nanoparticles are able to produce tubular protrusions for large enough adhesion strength. The tubular membrane wraps around the

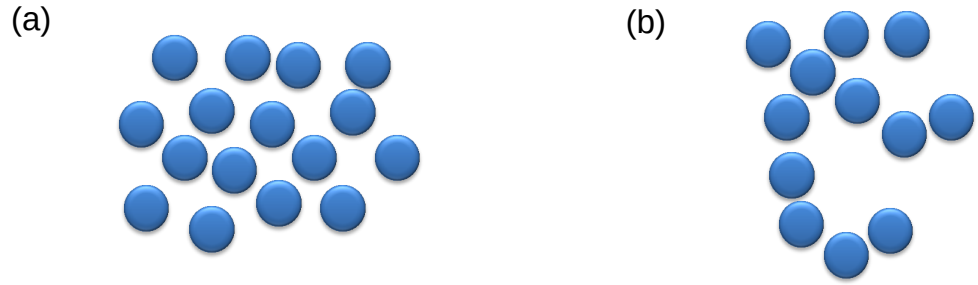

Figure 1.6: Illustration of nanoparticle arrangement: (a) hexagonal closed packing and (b) linear aggregates.

linearly aggregated nanoparticles, and the diameter of the tube roughly equals the one of nanoparticles [96, 6]. A similar tube formation process has been observed experimentally [42]. This is quite different from membrane tubes pulling out by optical tweezers or micropipette [88, 43, 94, 30] since the tube diameter is determined by membrane's mechanical property [35].

It is also possible for adhering nanoparticles to aggregate and produce collectively large membrane deformations, which the length scale of the produced structure is at least an order of magnitude larger than the size of the nanoparticles. Yu *et al.* studied the tubulations and pearling induced by cationic nanoparticles enclosd inside spherical phospholipids vesicles [119]. There are two stages in the whole process. First, the protrusion happens and grows into a tubular structure. The tube keeps growing until the whole vesicle becomes a long tubule. Note that the diameter of the tubule is at least an order of magnitude larger than the one of nanoparticles. Second, the pearling process starts from the tip of the tubule, which develops into a string of beads. Finally, the pearling structure breaks into many smaller spherical vesicles. A similar collective protrusion has been studied in computer simulations [91]. Caps and particles that modelled viruses are adsorbed on a particle-based membrane model. The deformations produced by each cap or particle overlap with each other and generate a large collective budding. However, for the pearling structure induced by nanoparticles, there is no theoretical explanation at this time. In Ch. 4, we proposed a coarse-grained model based on the grand canonical ensemble to study the mechanism of pearling.

In contrast to deformations induced by particle adhesion, different membrane structures can be produced by purely exploiting the excluded-volume interaction between nano-objects and membranes. For example, two nanoparticles inside a membrane with compa-

rable diameters are pushed away from or are bound to each other based on the surface tension of the membrane [24]. Also, a polymer chain, which can be regarded as a group of nanoparticles with strong correlations, trapped inside a membrane tube exhibits a similar response, which the polymer and the membrane adopt a globule structure as the surface tension increases[109, 16, 22]. Inspired by recent experiments [57, 81], our group studied the response of the polymer and the membrane when a polymer is trapped between a bilayer membrane and a flat surface [106, 107]. The results are discussed in Chs. 2 and 3.

1.5 Organization of thesis

In a broad sense, based on how the macromolecules interact with membranes, we study two types of systems in the thesis:

- *Passive interaction.* In Chs. 2 and 3, we study a polymer trapped between a bilayer membrane and a flat surface, which serves as a general model when polymers (such as DNAs or proteins) is trapped between a biological membranes (such as mucous membranes) and tissues (such as muscles or bones). Using Monte Carlo simulations, we show that the systems undergo discontinuous structural transitions by tuning either the adhesion strength between the membrane and the flat surface or the pressure difference between the compartment and the environment. Scaling theories were also developed to understand the behavior of the confined polymer chain.

- *Active interaction.* In Ch. 4, a theoretical model of the vesicle tubulation and pearling induced by nanoparticle adhesion is proposed and investigated. Based on the grand canonical ensemble, we construct a free energy model in the context of Helfrich model. By minimizing the free energy directly, we show that multiple nanoparticles with a proper adhesion strength and the deformation capability are able to induce protrusions, such as a bud, a tube, or a pearling structure. We also found a discontinuous structural transformation from a tubular structure to a pearling structure.

Finally, in Ch. 5, we summarize our findings and point out possible directions for our future studies.

Chapter 2

A self-avoiding polymer confined by a soft membrane adhering onto a flat wall

2.1 Introduction

A self-avoiding polymer in confinement is a classical topic in polymer physics [33], which is now understood relatively well. The problem of a polymer confined in soft walls made of fluid membranes contains even richer structures, however, is less well understood. For example, when a polymer is confined in a membrane tube with much smaller diameter than the polymer's size [16, 4, 22], its reduced entropy can overcome the membrane's elastic energy, driving the system to a drastically different, globular phase. In another example, when a polymer is confined near an originally flat soft surface by a short-ranged, attractive potential well, the net effects are modifications of the membrane's curvature [87, 72, 62]. Interesting structures emerge from the theoretical work, as well as recent experimental studies of related systems [40, 89, 109, 57, 104].

In this chapther, we study the system where a self-avoiding polymer is confined between two surfaces; one is made of lipid membrane bilayer and the other a hard wall, where the two surfaces attract to each other [see Fig. 2.1]. The theoretical model is inspired by a recent experiment conducted by Hisette *et al.* [57]. Using a Monte Carlo simulation scheme, we demonstrate that two distinctive states exist in the system: pancake and bud, shown in Fig. 2.2. These two states were referred to as the shallow- and balloon-bulges in a recent publication [108].

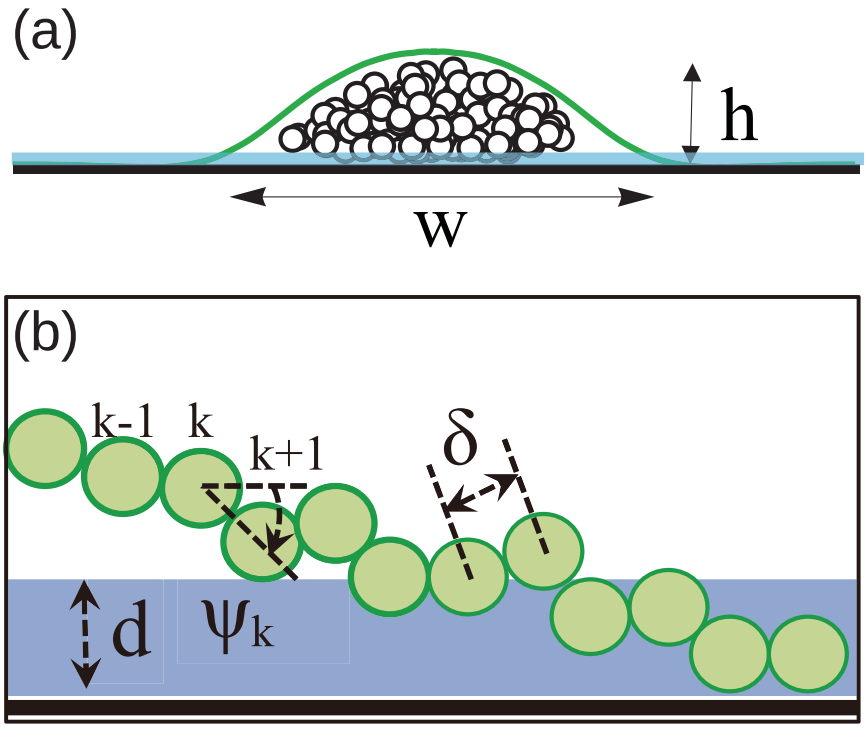

Figure 2.1: (a)Schematic representation of the system. (b) Discretization scheme of the membrane. The two-dimensional membrane surface are represented by [green] circles, and the [blue-] shaded region represents the adhesion interaction range. Reprinted with permission from Ref. [106]; copyright by The Royal Society of Chemistry.

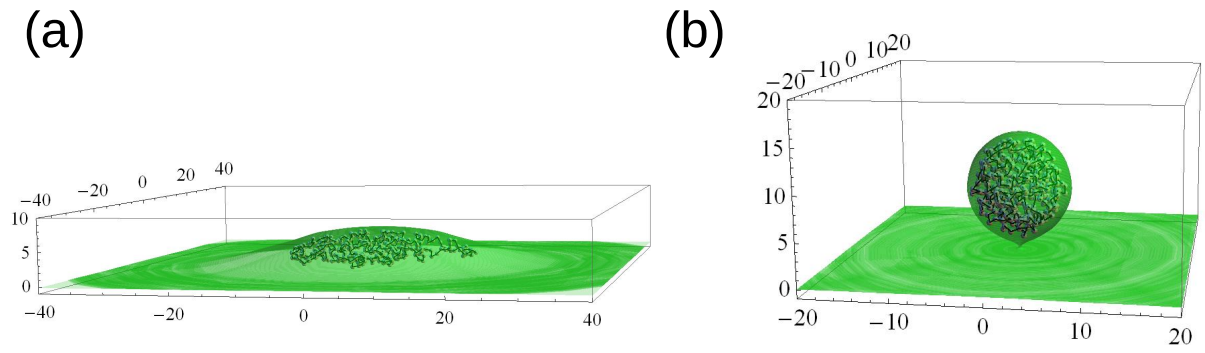

Figure 2.2: Simulation snapshots of a free polymer confined by the membrane-wall complex: (a) Pancake state observed in a system with $N = 400$, $\beta\gamma a^2 = 0.02$, and $\beta\sigma a^2 = 1.0$, and (b) bud state observed in a system with $N = 400$, $\beta\gamma a^2 = 2.0$, and $\beta\sigma a^2 = 1.0$. The scales of the plots are labelled in units of a. The system with a grafted polymer has an almost identical structure.

The scaling argument of a self-avoiding polymer confined in rigid objects, such as a hollow sphere or a tube, was advanced by de Gennes [33]. The key argument made in such a derivation is that the polymer free energy is dominated by the reduction of entropy due to confinement. In the current system, the entropy reduction can be compensated by the elastic energy of a deformed membrane. We develop a scaling theory following this consideration. Our Monte Carlo data agrees with the results from our scaling theory, however, disagrees with those predicted from the scaling theory by Thalmann *et al.* [108]; using the scaling argument, these authors studied exactly the same model but have estimated the polymer entropy in a different way from ours; detailed discussion can be found in Sect. 2.3 and Sect. 2.5.

A very interesting comparison of the current system is the droplet-induced budding transition of an originally flat membrane that is wetted by one of two demixing fluids [73, 66]. The adhesion energy between the membrane and the hard surface considered in the present study plays a similar role as the interfacial energy between the two demixing fluids[66].

The discussion is organized as follows. The basic model is introduced in Sect. 2.2, and we propose a scaling theory for the current system, predicting different scaling results in contrast with those by Thalmann *et al.*[108] in Sect. 2.3. The numerical scheme of the membrane and the polymer is discussed in Sect. 2.4. In Sect. 2.5, we discuss the

phase transition induced by the adhesion energy. Also, we compare the simulation data with scaling predictions, examining the validity of the assumptions used in making the predictions.

2.2 Model

The current model consists of a single self-avoiding polymer covered by a deformable fluid membrane which adheres to a hard surface [see Fig. 2.1(a)]. The free energy of the system has three major contributions: the polymer's free energy, $F_{\rm poly}$, the membrane's free energy, $F_{\rm mem}$, and the adhesion energy, $E_{\rm ad}$.

First, the free energy of the polymer, $F_{\rm poly}$, is composed of the excluded-volume interaction between monomers, which swells the overall conformation of the polymer chain, and the conformational entropy, which is reduced when the polymer is confined between the membrane and the substrate. Both factors depend on the monomer number N of the polymer and produce an osmotic pressure of the polymer against the confinement.

Next, for a two-dimensional fluid membrane, the Helfrich energy [55] can be written as,

$$E_{\rm mem} = 2\kappa \int M^2 \, dA + \sigma \Delta A, \tag{2.1}$$

where M is the local mean principal curvature of the surface element dA, and $\Delta A = \int dA - \int' dA$ is the excess area between the stretched surface $\int dA$ and the originally flat, adsorbing surface $\int' dA$. The bending modulus κ controls the curvature deformation on the membrane, and the surface tension σ describes the cost of stretching the membrane's surface. For simplicity, we did not include the spontaneous curvature and Gaussian bending energy contribution in this expression [100, 78].

Finally, the excess adhesion energy is given by

$$E_{\rm ad} = \gamma \int'' dA, \tag{2.2}$$

where $\int'' dA$ is the non-adhered area on the substrate. The parameter γ describes the cost of detaching unit area of the membrane from the substrate. This term effectively accounts for the adhesion produced by the surface ligand-receptor binding which has been reported in experiments. The size of γ in the experiment[57] is of the order of magnitude of $10^2 k_B T$ per 100 nm^2, where k_B is the Boltzmann constant and T the room temperature. Possible

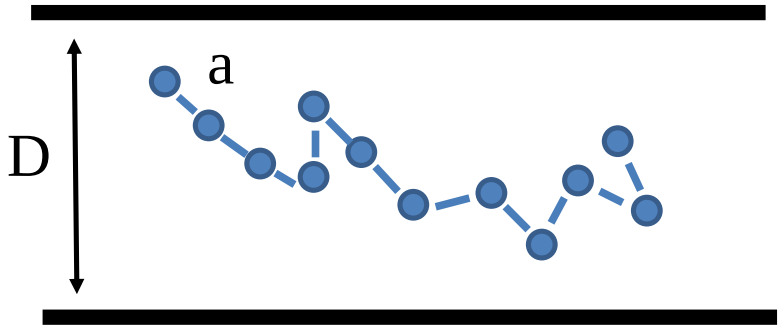

Figure 2.3: The confinement length D is much larger than the polymer segment length a.

interactions between the polymer and the interior wall of the confining membrane, and between the polymer and the hard wall surface, are all ignored except for the excluded volume interaction. The introduction of adhesion energy per unit area was previously considered in modeling systems consisting of a membrane interacting with adsorbing rigid particles or with a hard-wall environments [102, 36, 115, 79, 80, 31, 24, 77, 25, 21].

The overall free energy for the system,

$$F = F_{\text{poly}} + F_{\text{mem}} + \langle E_{\text{ad}} \rangle, \tag{2.3}$$

contains four parameters: N, $\beta\kappa$, $\beta\sigma a^2$, and $\beta\gamma a^2$, where $\beta = 1/k_B T$. In this and the following chapters, $\langle \cdots \rangle$ denotes the average taken in a canonical ensemble, which amounts to considerations of all possible configurations of the confined polymer and the confining membrane. We use the Monte Carlo simulation method to study the system by moving both polymer and membrane.

2.3 Scaling analysis

Before discussing the numerical results obtained from Monte Carlo simulation, we would like to present scaling arguments of the current model to provide some physical insights of the system. In a previous study, Thalmann *et al.* explored a similar model using

scaling arguments[108]. In this section, following a similar approach, we develop several different scaling relations based on different assumptions about the behavior of the trapped polymer, and the scaling relations are compared with the Monte Carlo data to verify those assumptions in Sect. 2.5.

In our current model of the polymer, there are two important factors determining the free energy of it: One is the excluded-volume interaction between monomers, and the other one is the confinement entropy induced by the compression of the polymer chain. Here we briefly review how to estimate the free energy of the polymer chain using scaling concepts. More detailed discussions can be found in Ref. [33].

For the excluded-volume interaction, we consider a polymer chain with N segments confined to a volume V. The concentration of the segment, ρ, is

$$\rho \sim \frac{N}{V}. \tag{2.4}$$

If each monomer occupies a volume u, the free energy due to the excluded-interaction contributed by just one monomer is proportional to $u\rho$. Thus, for N monomers, the total free energy contributed by the excluded volume, F_{ex}, is

$$\beta F_{\text{ex}} \sim uN^2/V. \tag{2.5}$$

For the confinement entropy, we consider a polymer chain trapped inside a slit separated by a distance D, where D is much larger than the polymer segment length a, as illustrated in Fig. 2.3. Here the estimated entropy ΔS is a dimensionless number, so we expect its value to be proportional to the ratio of the relevant length quantities, R_{ex} and D, in the form of

$$\Delta S \sim \big(\frac{R_0}{D}\big)^{\alpha}, \tag{2.6}$$

where $R_0 \sim N^{\nu}$ is the mean end-to-end distance of a polymer chain. Intuitively, the leading term of ΔS should be linear in the polymer segment number N. Thus, we infer that $\alpha = 1/\nu$, and the free energy induced by the compression of the polymer chain can be written as

$$\beta F_{\text{com}} \sim N\big(\frac{a}{D}\big)^{1/\nu}, \tag{2.7}$$

where $\nu = 1/2$ for a polymer without the excluded-volume interaction; in contrast, $\nu = 3/5$ for the one with the excluded-volume interaction[33].

Now we are ready to analyze the model using scaling concepts. Two configuration settings will be discussed: a balloon-like bud state and a pancake state in the strong surface tension limit.

2.3.1 Scaling of bud state

We assume that the bud state has a spherical shape, so the bending energy becomes almost a constant,

$$2\kappa \int M^2 \, dA \sim \kappa. \tag{2.8}$$

Dropping a numerical coefficient, we can write the membrane surface area of the bud as

$$\Delta A \sim h^2, \tag{2.9}$$

where h is the globular size.

Next, we consider two different assumptions of writing down the free energy for the confined polymer. Making the excluded-volume interaction as the main contribution, we can write the polymer's free energy as

$$\beta F_{\text{poly}} \sim \frac{uN^2}{h^3} \tag{2.10}$$

where we used the estimation for the excluded volume interaction of a self-avoiding polymer. For the total free energy of the system, we then have

$$\beta F \sim \beta\kappa + \beta\sigma h^2 + u\frac{N^2}{h^3}. \tag{2.11}$$

Minimizing the free energy with respect to h gives the following scaling relation,

$$h \sim \sigma^{-1/5} N^{2/5}. \tag{2.12}$$

Hence

$$\langle \Delta A \rangle \sim \sigma^{-2/5} N^{4/5}, \tag{2.13}$$

which is discussed in Sect. 2.5.2.

Another possible way of examining the polymer free energy would be to take the entropy dominating assumption, which was the approach taken by Thalmann *et al.*[108]. The polymer's free energy then becomes

$$\beta F_{\text{poly}} \sim N\left(\frac{a}{h}\right)^{5/3}. \tag{2.14}$$

Minimizing the total free energy,

$$\beta F \sim \beta\kappa + \beta\sigma h^2 + N\left(\frac{a}{h}\right)^{5/3}, \tag{2.15}$$

with respect to h yields

$$h \sim N^{3/11}\sigma^{-3/11}. \tag{2.16}$$

Hence,

$$\langle \Delta A \rangle \sim \sigma^{-6/11}N^{6/11}. \tag{2.17}$$

The justification of dropping (2.14) in (2.11) can be self-consistently checked. Using (2.12) in (2.10) we have $F_{\text{poly}} \sim \sigma^{3/5}N^{4/5}$, whereas using (2.12) in (2.14) we have $F_{\text{poly}} \sim \sigma^{1/3}N^{1/3}$; the former is much larger than the latter in the large N limit; therefore, the contribution in (2.14) can be dropped. Likewise, if we were to take the result from the entropy dominating assumption (2.16) in (2.11) we would have $F_{\text{poly}} \sim \sigma^{9/11}N^{13/11}$, whereas using (2.16) in (2.14) we have $F_{\text{poly}} \sim \sigma^{5/11}N^{6/11}$; the former is still much larger than the latter in the large N limit; therefore, dropping (2.10) in the analysis of (2.15) is incomplete. From this comparison, we can already conclude that the scaling behavior, (2.13), is more physical. Indeed, in Sect. 2.5, we will show that the Monte Carlo data agrees with Eq. (2.13), not Eq. (2.17).

2.3.2 Scaling of pancake state in the strong surface tension limit

The pancake conformation is described by two measurements: w that measures the size of the circular projection on the xy plane and h the height in the z direction. On the basis that detached portion is approximated as a part of the sphere, we can estimate the curvature $1/R \sim h/w^2$ and the excess surface area $\Delta A \sim h^2$. This gives

$$E_{\text{mem}} \sim \kappa\frac{h^2}{w^2} + \sigma h^2. \tag{2.18}$$

In the pancake state $w/a \gg 1$; in most parameter region considered in this study, $\kappa \ll \sigma w^2$, hence the first term in the above equation can be dropped.

The free energy of the confined polymer, which experiences a large compression in the z direction, can be written as [33]

$$\beta F_{\text{poly}} \sim u\frac{N^2}{w^2 h} + N\left(\frac{a}{h}\right)^2. \tag{2.19}$$

This gives rise to the total free energy for the system,

$$\beta F \sim \beta\sigma h^2 + \beta\gamma w^2 + u\frac{N^2}{w^2 h} + N\left(\frac{a}{h}\right)^2. \tag{2.20}$$

In the weak adhesion region, minimizing the total free energy with respect to w and h, we obtain the following scaling relations,

$$w \sim \sigma^{1/16}\gamma^{-1/4}N^{7/16}, \tag{2.21}$$

and

$$\frac{w}{h} \sim \sigma^{5/16}\gamma^{-1/4}N^{3/16}. \tag{2.22}$$

Both agree with our numerical data, as discussed in Sect. 2.5.3.

Another approach was taken by Thalmann *et al.*[108] for the scaling analysis, which assumed the entropy dominates the polymer free energy and incorporated a logarithmic correction factor into the surface tension term. The result of this analysis gives

$$w \sim \sigma^{5/22}\gamma^{-1/2}N^{3/11}, \tag{2.23}$$

and an N-independent

$$\frac{w}{h} \sim \sigma^{1/2}\gamma^{-1/2}, \tag{2.24}$$

which is different from our scaling analysis discussed in the above. In Sect. 2.5.3, we showed that the Monte Carlo data disagrees with Eq. (2.23) and (2.24).

2.3.3 Scaling of phase transition boundary

It is possible to estimate the transition boundary by plugging the the scaling results we found in the above into the corresponding free energy equations and equating them. For the bud state, plugging Eq. (2.12) into Eq. (2.11), we have

$$\beta F_{\text{bud}} \sim \sigma^{3/5}N^{4/5}. \tag{2.25}$$

For the pancake state, plugging Eqs. (2.21) and (2.22) into Eq. (2.20), we get

$$\beta F_{\text{bud}} \sim \sigma^{1/8}N^{7/8}\gamma^{1/2}. \tag{2.26}$$

Equating the two free energy expressions in the above, we obtain a scaling relation of the transition boundary:

$$\gamma* \sim \sigma^{19/20}N^{-3/20}, \tag{2.27}$$

where $\gamma*$ is the value of γ at the transition point. This relation shows that increasing σ also increases $\gamma*$ while increasing N decreases $\gamma*$. We shall see this result qualitatively agrees with the numerical results in Sect. 2.5.

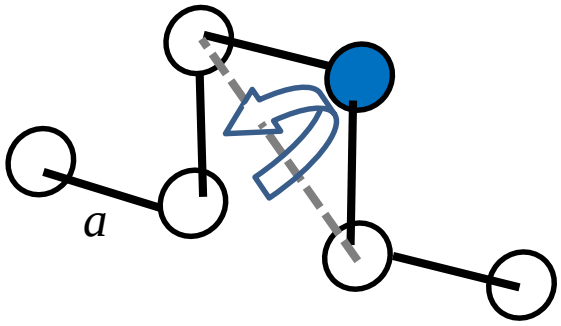

Figure 2.4: The monomer position is updated through rotating around the axis formed by the adjacent monomers.

2.4 Monte Carlo scheme

A self-avoiding polymer is modelled as a freely rotating chain of $N-1$ bonds, each of length a. The bonds connect N monomers linearly, where every monomer has a hard-sphere radius D. The polymer chain is subjected to the excluded volume condition between the monomers as well as between the monomers and the nodes of the membrane. To update the configuration of the polymer chain, a randomly selected monomer is rotated about the vector connecting the two adjacent monomers along the chain (Fig. 2.4). A polymer chain can either be grafted or move freely in space; both cases are examined.

In principle, a full scale membrane simulation that directly uses two-dimensional mesh is possible; such a simulation, however, is computationally expensive. To efficiently implement the Monte Carlo simulation, the deformable membrane is considered to have a rotational symmetry about the z-axis in a cylindrical coordinate system. As an approximation in this work, the dependence of the shape fluctuation on the azimuthal angle is suppressed [22, 23]. The approximation can be justified by the fact that for large $\beta\kappa$, the membrane statistics is basically dominated by the bending energy, not thermal fluctuations. Indeed, in recent theoretical studies of systems of membrane-macromolecule interaction, the bending energy itself, not the membrane's free energy, is directly used for structural analysis [102, 36, 115, 79, 80, 31, 24, 77, 25, 21]. We take this point of view in this work, by assuming $F_{\mathrm{mem}} \simeq \langle E_{\mathrm{mem}} \rangle$. The simplification reduces the computational complexity of the model and allows for the simulation of large systems. In a general sense, the membrane portion of the Monte Carlo scheme in this study, as well as in the previous works[22, 23],

is used to direct the system to find an optimal shape for the membrane-energy minimum.

The membrane shape is described completely by $[r(s), z(s)]$, where r is the radial variable and s an arc variable measured from the symmetry axis. The parameterized version of the energy associated with the membrane, Eq. (2.1), can be written as [101, 36],

$$\begin{aligned} E_{\text{mem}} = \pi\kappa \int_0^\infty r(\dot{\psi} + \frac{\sin\psi}{r})^2 \, ds \\ + 2\pi\sigma \int_0^\infty r(1 - \cos\psi) \, ds, \end{aligned} \tag{2.28}$$

where $\psi(s)$ is the angle between the tangent direction of the shape curve and the substrate surface; the dot on a symbol implies a derivative with respect to s.

The length scale in the system is rendered dimensionless by consideration of a scaling factor $1/a$. In the simulation, the arc variable s/a is uniformly discretized into m nodes, each hosting a hard bead with a diameter δ shown in Fig. 2.1(b). The above integrations are then replaced by summations. To update the configuration of the membrane, a randomly selected ψ_k is modified by a small random value. The coordinates $[r(s_i)/a, z(s_i)/a]$, with $k+1 \leq i \leq m$, are changed accordingly. Then, the configuration is translated along the z-axis such that the end node is in close contact with the substrate. In other words, the end node is vertically fixed at the level of the substrate and can only move in the horizontal direction; this condition is crucial to updating the membrane shape efficiently.

A node of the discretized arc variable is considered to be in an adhesion position near the substrate if the center of the node is within the interaction range d, as illustrated in Fig. 2.1(b). We measure the diameter w of the disk area that is free from membrane adhesion. The adhesion energy can be calculated as

$$E_{\text{ad}} = \gamma\pi w^2/4, \tag{2.29}$$

which assumes the azimuthal symmetry.

The parameters $D = 0.9a$, $\delta = 0.2a$, and $d = 0.3a$ were selected. Every Monte Carlo step consists of N attempts of moving a randomly selected monomer and $m/10$ attempts of changing a randomly selected angle ψ_k associated with the membrane nodes; The acceptance of the attempt was then evaluated based on the Metropolis algorithm for the statistical weight $\exp[-\beta(E_{\text{mem}} + E_{\text{ad}})]$. In the present study, $\beta\kappa$ is fixed at 16, which corresponds to the order of magnitude in the actual biological systems. Under this condition, the model is completely controlled by three parameters: N, $\beta\sigma a^2$, and $\beta\gamma a^2$. More than 6×10^6 Monte Carlo steps were used for computing a data point corresponding to a given set of the parameters; also, an equal number of the steps was used for equilibration.

2.5 Numerical results and discussion

In this section, we present a phase diagram of the discontinuous budding transition. The physical properties of each state are then examined in comparison with scaling theories.

To measure the conformation of the system, two ratios of the gyration of polymer, ξ_{xy} and ξ_z, are measured in the simulation,

$$\xi_{xy} \equiv \langle S_{xy}^2 \rangle / \langle S_{xy,0}^2 \rangle, \tag{2.30}$$

and

$$\xi_z \equiv \langle S_z^2 \rangle / \langle S_{z,0}^2 \rangle, \tag{2.31}$$

where $\langle S_{xy}^2 \rangle$ and $\langle S_z^2 \rangle$ are the mean square radii of gyration measured in the xy-plane and along the z-axis respectively, and $\langle S_{xy,0}^2 \rangle$ and $\langle S_{z,0}^2 \rangle$ the counterparts of a free polymer. For the membrane conformation, the mean width-height ratio w/h, the mean non-adhered disk area $\pi w^2/4a^2$, the mean excess area $\Delta A/a^2$, and the mean reduced bending energy,

$$E_\mathrm{b}/\kappa = 2 \int M^2 \, dA \tag{2.32}$$

were measured.

2.5.1 Phase transition

In the examined region of the parameter space, we observed two distinct states: pancake and bud, as illustrated in Fig. 2.2. Out of the three reduced parameters, N, $\beta\sigma a^2$, and $\beta\gamma a^2$, we first examine the phase behavior by fixing $\beta\sigma a^2$. The transition between these two phases can be viewed by varying the adhesion energy or the polymer length.

Figs. 2.5, 2.6, and 2.7 show several features of the phase transition. First of all, as N increases, the value of $\beta\gamma a^2$ at the transition point, γ^*, drops [Fig. 2.5]; a larger N normally implies a higher osmotic pressure. When the system is in the pancake state, the dimensions of the overall polymer conformation are compressed in all directions, along the xy plane and the z direction, which is demonstrated by small ratios, ξ_{xy} and ξ_z, in Fig. 2.6(a) and (b). As $\beta\gamma a^2$ increases, the membrane prefers more contact with the wall hence reduces the noncontact disk size $\pi w^2/4a^2$ [Fig. 2.7(a)], through the membrane-wall attraction, Eq. (2.29); this further minimizes the entropy of the polymer chain and increases the osmotic pressure. Therefore, both polymer's osmotic pressure and adhesion energy prefer the budding transition.

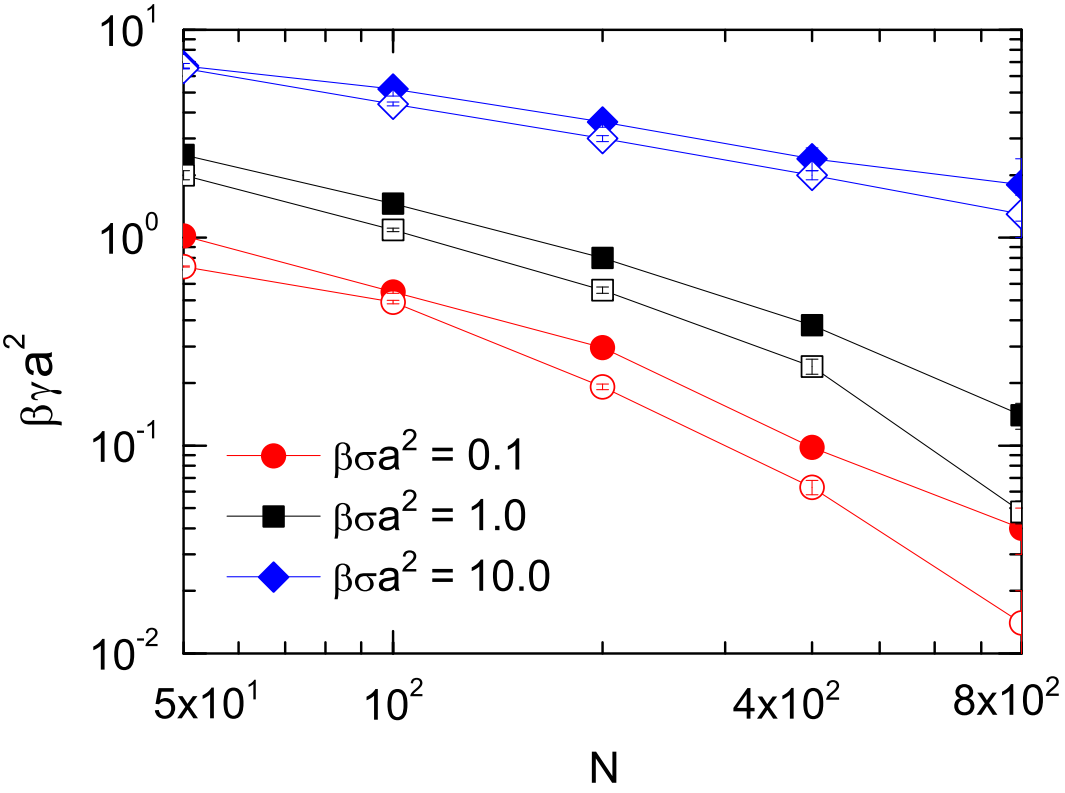

Figure 2.5: Phase boundaries between the pancake state (lower left region) and the bud state (higher right region) for various values of $\beta\sigma a^2$. The symbols are the transition points determined by the Monte Carlo simulation, and lines are the estimated boundary. An abrupt transition from the pancake state to the bud state occurs, as the phase boundary is crossed. Filled and Open symbols correspond to grafted and free polymers under confinement. Reprinted with permission from Ref. [106]; copyright by The Royal Society of Chemistry.

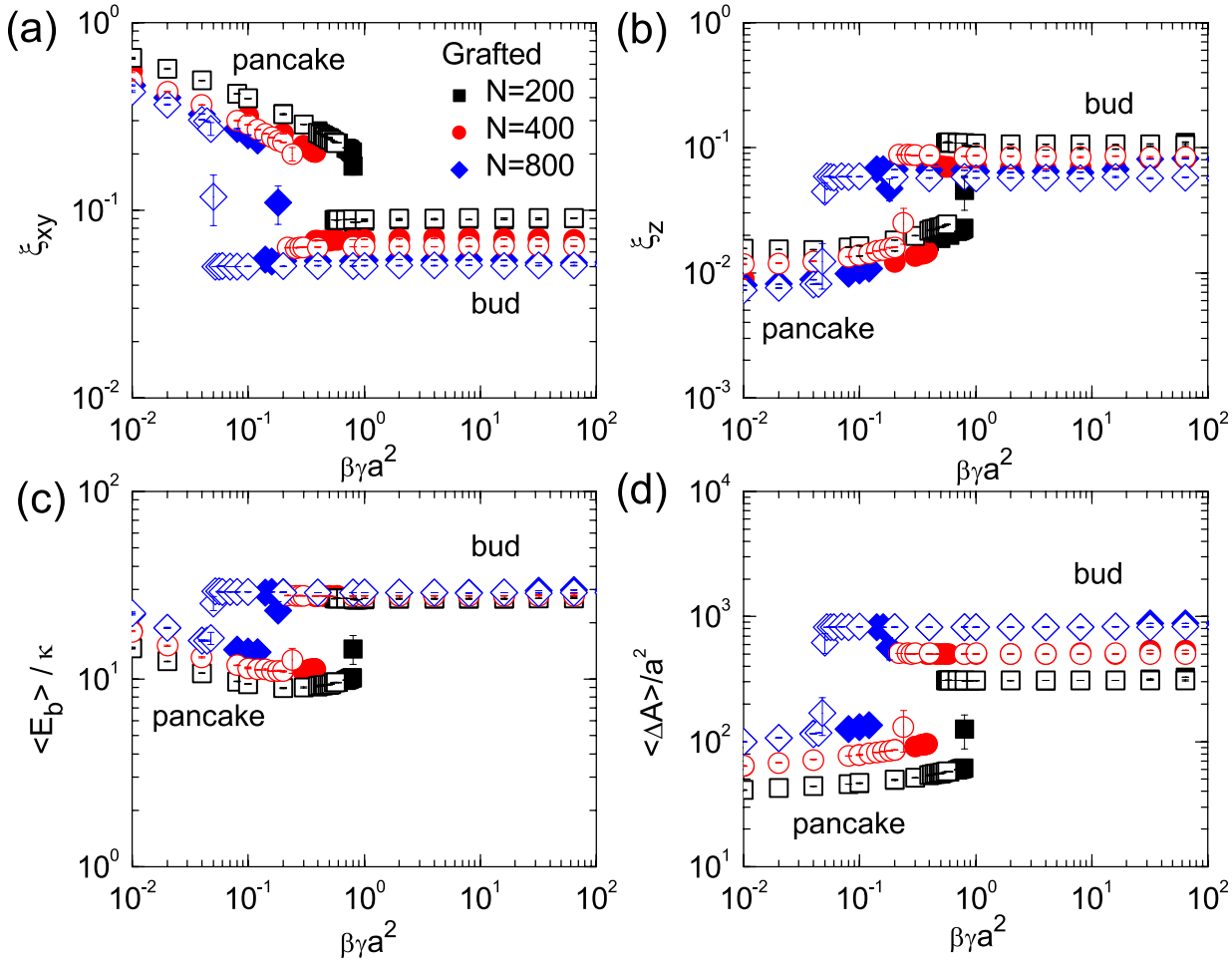

Figure 2.6: Data obtained from our Monte Carlo simulations for various physical quantities examined by fixing $\beta\sigma a^2 = 1.0$. All open symbols correspond to the situation that a free polymer is confined, whereas filled symbols the situation a grafted polymer is confined. Ratios of the polymer's gyration dimensions in xy-plane and along the z-axis, defined in Eqs. (2.30) and (2.31), are displayed in (a) and (b). The reduced bending energy, $\langle E_{\rm b}\rangle/\kappa$, and the excess area of the membrane after being stretched to cover the polymer, $\langle \Delta A\rangle/a^2$, are displayed in (c) and (d), respectively. Reprinted with permission from Ref. [106]; copyright by The Royal Society of Chemistry.

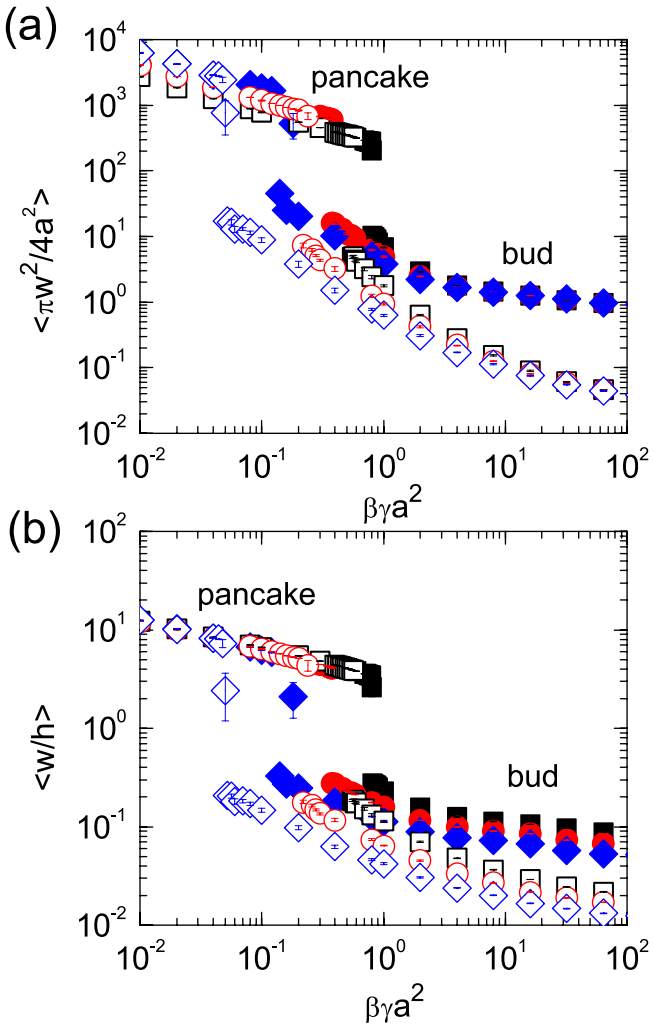

Figure 2.7: Data obtained from our Monte Carlo simulations by fixing $\beta\sigma a^2 = 1.0$. All open symbols correspond to the situation that a free polymer is confined, whereas filled symbols the situation a grafted polymer is confined. The nonadhering surface-wall area, $\langle \pi w^2/4a^2 \rangle$, is displayed in (a). The aspect ratio of a conformation, $\langle w/h \rangle$, is displayed in (b). Reprinted with permission from Ref. [106]; copyright by The Royal Society of Chemistry.

Passing through the transition point, an abrupt transition from the pancake state to the bud state occurs. Although it takes more bending and surface tension energy for the membrane to form the bud shaped conformation, the nonadhered disk size is reduced as preferred by the adhesion energy; as a result the compressed polymer regains a globular symmetry as indicated by comparable sizes in ξ_{xy} and ξ_z. The free energy of the compressed polymer is affected by two significant factors: the monomer-monomer excluded volume interaction and the confinement entropy. It is intriguing to ask which dominates in each state. We will explore this question in the next two sections.

Another feature in Fig. 2.5 is that as the membrane becomes more rigid, i.e. through increasing $\beta\sigma a^2$, it takes higher pressure to jump to the bud state. Furthermore, in the limit of $\beta\sigma a^2 \to \infty$, the membrane becomes a rigid plate. In this limit, there is no bud state, and the grafting condition becomes irrelevant. In the opposite limit of $\beta\sigma a^2 \to 0$, the budding transition can take place much more easily.

Finally, a difference between systems containing a confined *free* polymer or a *grafted* polymer can be viewed in Fig. 2.5 by comparing unfilled and filled symbols. The most visible difference is the shifted phase boundary, γ^* as a function of N; other general qualitative behavior remains the same. Away from the immediate transition region, open and filled symbols merge in Fig. 2.6; the polymer's dimensions and membrane's energies all stay the same for both cases: grafted or free, in the pancake and bud states. In the strong adhesion limit, the membrane around the bottom of the bud closes. In the grafted-polymer case, the size of the unadhered disk is restricted to at least one diameter of the grafted monomer, while in the free-polymer case, the bottleneck can close. This causes the divergent branching of w-related properties in the two cases, in the strong adhesion limit, as seen in Fig. 2.7.

2.5.2 Properties of the bud state

One distinctive feature of the bud states is that at the strong adhesion limit, the wrapping membrane forms a nearly perfect spherical shape. Because the non-adhered disk has a vanishing size in the bud states [see Fig. 2.7(a)], ξ_{xy}, ξ_z, and $\langle \Delta A \rangle / a^2$ are all independent of $\beta\gamma a^2$, but dependent on N and $\beta\sigma a^2$, which is directly related to the size of the bud; this feature is shown in Figs. 2.6(a), (b), and (d) at large values of $\beta\gamma a^2$. The reduced bending energy $\langle E_{\rm b} \rangle / \kappa \sim 8\pi$ is a particular example. Because of the length-scale invariance of the bending energy, $\langle E_{\rm b} \rangle / \kappa$ maintains almost exactly the same in this limit [Fig. 2.6(c)], independent of N, $\beta\sigma a^2$, $\beta\gamma a^2$; the value is approximately that of a perfect sphere.

Now, the scaling dependence of $\langle \Delta A \rangle$ on N and σ deserves a more careful examination.

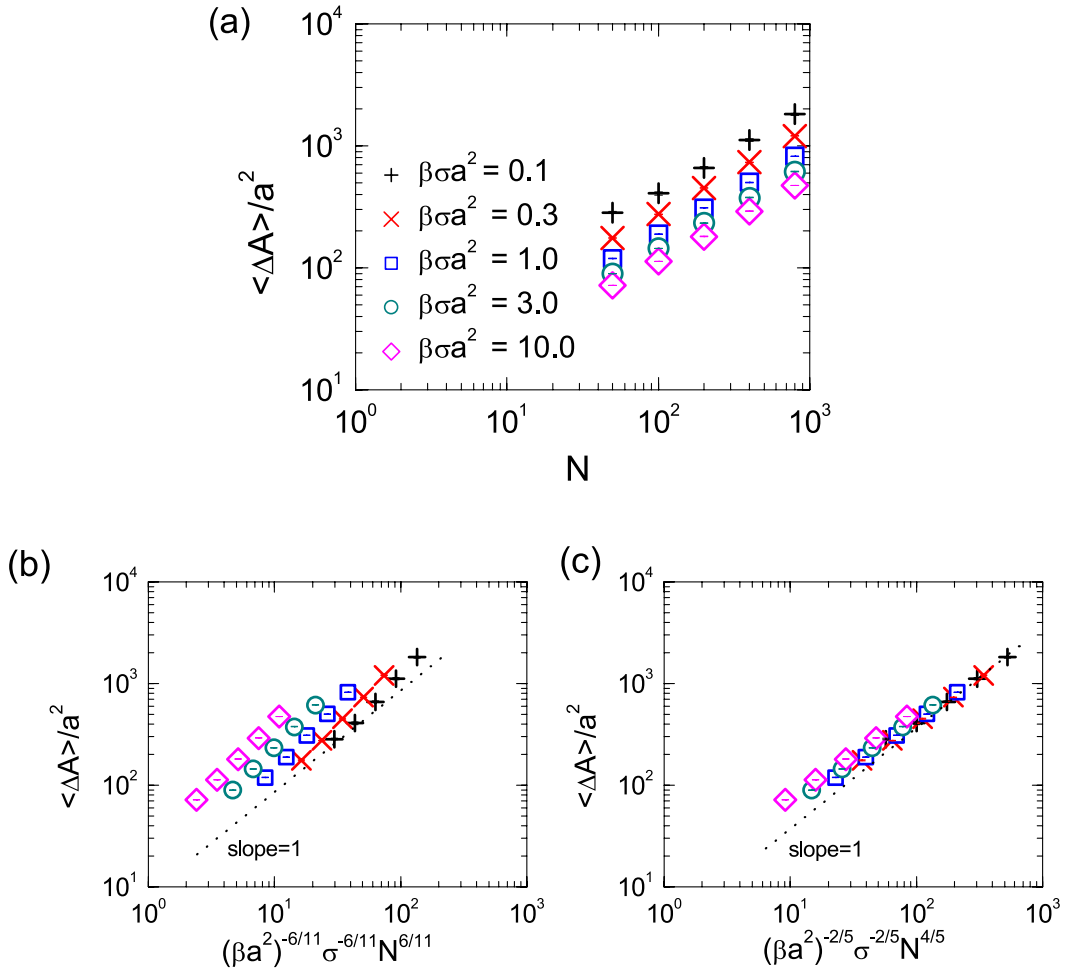

Figure 2.8: (a) Excess area of the bud states, $\langle \Delta A \rangle / a^2$, in comparison with the unperturbed, flat membrane, as a function of N and $\beta\sigma a^2$ at $\beta\gamma a^2 = 8.0$. Plot (b) rearranges the horizontal axis according to the result from a previous scaling theory, Eq. (2.17). Plot (c) rearranges the horizontal axis according to the result, Eq. (2.13), from a new scaling theory presented in Sect. 2.3.1. Dotted lines demonstrate the anticipated scaling behavior in both cases. Reprinted with permission from Ref. [106]; copyright by The Royal Society of Chemistry.

The raw data is shown in Fig. 2.8(a) where the dimension of the bud state shrinks as surface tension rises. Based on the scaling analysis, two different scaling relations can be derived. In an entropy-dominating scenario, according to Thalmann *et al.*[108], we have

$$\langle \Delta A \rangle \sim \sigma^{-6/11} N^{6/11}. \tag{2.17}$$

This is demonstrated in Fig. 2.8(b) by the dotted line. As we can see, the Monte Carlo simulation data disagrees with the prediction. In an excluded-volume dominating scenario, we have arrived at a new scaling relation in Sect. 2.3.1,

$$\langle \Delta A \rangle \sim \sigma^{-2/5} N^{4/5}. \tag{2.13}$$

The dotted line in Fig. 2.8(c) demonstrates this scaling behavior. Our Monte Carlo simulation results, in particular those with larger N, collapse to the dotted line asymptotically. This result validates the excluded-volume dominating physical picture presented in Sect. 2.3.1.

Our numerical data also demonstrates the expected $\xi_z \sim \xi_{xy} \sim \langle \Delta A \rangle / N^{6/5}$ for the globular conformation, although ξ_{xy} and ξ_z are independently measured from our simulations. A detailed comparison is omitted here.

2.5.3 Properties of the pancake state

The pancake conformation can be characterized by the aspect ratio $\langle w/h \rangle$ and the area of the nonadhered area, $\langle \pi w^2/4a^2 \rangle$. Both depend on the three parameters in the model, N, $\beta\sigma a^2$, and $\beta\gamma a^2$. The raw data taken from the measurements conducted in our Monte Carlo simulations can be viewed in Figs. 2.9(a) and 2.10(a).

We compare the simulation data with two scaling theories. On the basis of the entropy-dominating scenario, Thalmann *et al.* previously arrived at [108],

$$w^2 \sim \sigma^{5/11} \gamma^{-1} N^{6/11}. \tag{2.23}$$

and

$$w/h \sim \sigma^{1/2} \gamma^{-1/2}, \tag{2.24}$$

The dotted lines in Figs. 2.9(b) and 2.10(b) demonstrate this scaling behavior. The slope and scattering of the simulation data disagree with this prediction.

We have re-developed a new scaling theory in Sect. 2.3.2 for the pancake state, where we treated the polymer excluded volume and entropy as being equally important. According to Appendix 2.3.2, we now have

$$w^2 \sim \sigma^{1/8} \gamma^{-1/2} N^{7/8}, \tag{2.21}$$

$$w/h \sim \sigma^{5/16}\gamma^{-1/4}N^{3/16}, \tag{2.22}$$

which are different from the predictions given by Thalmann *et al.*[108]. These scaling relations are demonstrated in Figs. 2.9(c) and 2.10(c) by dotted lines. Our simulation results, especially those with large N and $\beta\sigma a^2$, collapse to the dotted line asymptotically. This agreement verifies the physical picture presented in Sect. 2.3.2. The large N (hence large w) and $\beta\sigma a^2$ requirement was the assumption made in driving these scaling relations.

2.6 Summary

In summary, we developed a Monte Carlo procedure that follows the Helfrich energy for the description of a soft membrane surface and incorporates an additional adhering energy between the membrane and a hard-wall surface. We show that as a self-avoiding polymer is confined between the membrane and the hard wall, the system undergoes a discontinuous structural transition between two states, pancake and bud. The scaling behavior of the Monte Carlo measurements in the bud and pancake states is analyzed carefully in light of the analytic expressions obtained previously and in the Appendices. Our new scaling theory fully agrees with the Monte Carlo simulation data, showing the importance of incorporating the excluded volume interaction in a scaling theory for this type of systems. The results presented in this work may provide insights to the budding mechanism and stimulate experimentalists to further study the mechanical properties of polymer-confining soft membranes.

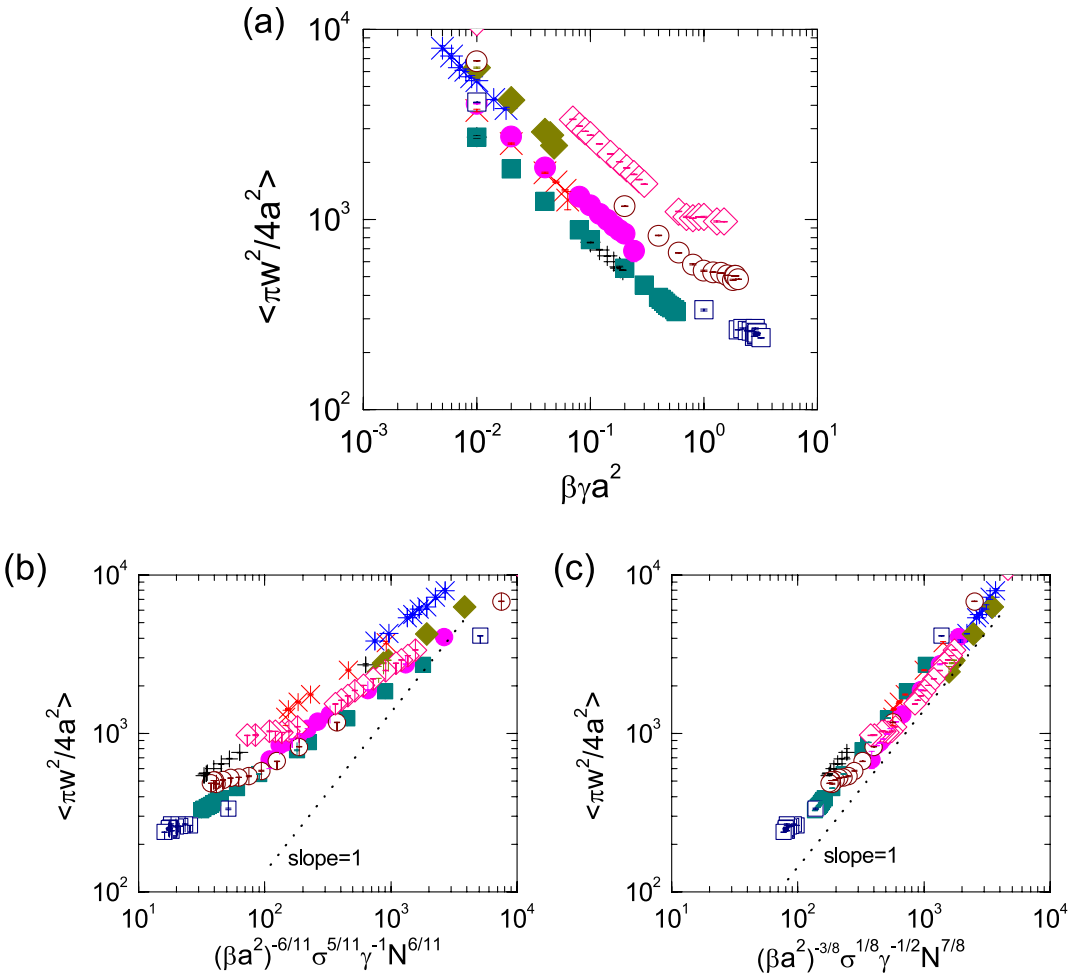

Figure 2.9: (a) Aspect ratio, $\langle w/h \rangle$, measured from the Monte Carlo simulation for the pancake state, as a function of $\beta\gamma a^2$ for various N and $\beta\sigma a^2$. The horizonal axis is re-scaled in (b), in reference to a previous scaling-theory result, Eqs. (2.24), according to Thalmann *et al.*[108]. The horizontal axis is re-scaled in (c), following the new scaling behavior, Eqs. (2.22), predicted in Sect. 2.3.2. Reprinted with permission from Ref. [106]; copyright by The Royal Society of Chemistry.

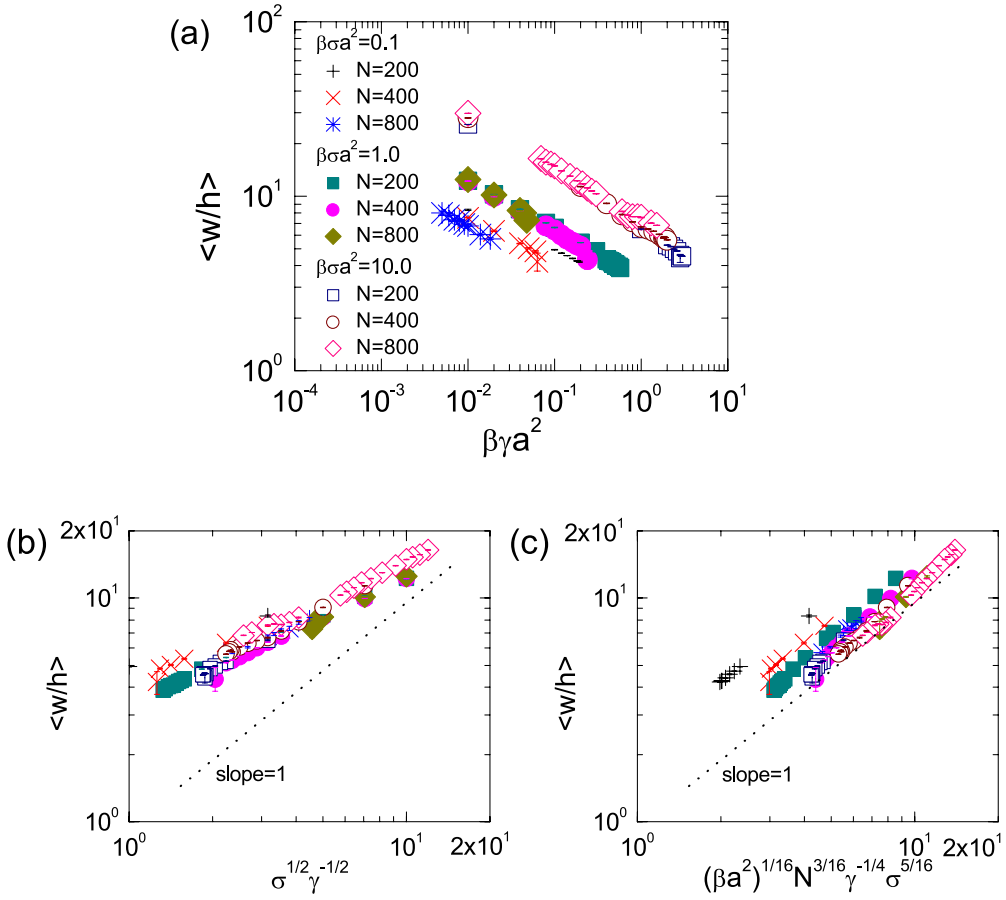

Figure 2.10: (a)Nonadhered wall area, $\langle \pi w^2/4a^2 \rangle$, measured from the Monte Carlo simulation for the pancake state, as a function of $\beta\gamma a^2$ for various N and $\beta\sigma a^2$. The horizonal axis is re-scaled in (b), in reference to a previous scaling-theory result, Eq. (2.23), according to Thalmann *et al.*[108]. The horizontal axis is re-scaled in (c), following the new scaling behavior, Eq. (2.21), predicted in 2.3.2. Reprinted with permission from Ref. [106]; copyright by The Royal Society of Chemistry.

Chapter 3

Pressing soft membrane to a self-avoiding polymer against a flat wall

3.1 Introduction

Polymers and membranes are ubiquitous in biological systems. It is known that the interaction between the two produces surprisingly rich and complex phenomena. For example, a membrane-anchoring polymer can modify the membrane curvature through the entropic force [12, 3]. More drastically, polymers with hydrophobic segments which anchor to the lipid bilayer to generate a spontaneous curvature can induce tubulation or even pearling if the polymer concentration is enough high [111, 110]. A polymer adsorbed onto a soft membrane provides another example of intertwining membrane curvature and polymer; the polymer could deform the membrane shape [87, 72, 62] at the right physical conditions. The important ingredients that need to be considered here are: polymer's entropy, membrane's bending and surface-tension energies, and the essential interactions in the system.

With the presence of the exclude-volume effects between the polymer and membrane, some confinement systems demonstrate interesting conformation properties. A polymer chain trapped inside a membrane tube can adopt a globular structure at a high surface tension [109, 16, 22]; a vesicle adhering onto a substrate, which confines a polymer between the membrane and substrate surfaces, induces a budding transition when the adhesion is strong enough [57, 108, 106]. Beyond the conformation modification, a recent *in vitro* experiment exploits the excluded-volume effects to scrape and staple DNA chains by vesicles

to study the chain topological structure [81].

In this chapter, we develop a simple model to explore yet another interesting structural change in a polymer-membrane complex. We consider pressing a polymer chain confined between a soft membrane and a hard surface through a pressure on the membrane surface. This can be realized in an experiment by pressing a vesicle on a grafted or confined polymer, as shown in Fig. 3.1. Under such a simple arrangement, we predict that a discontinuous phase transition is possible, from a confined state to a strongly confined state [Fig. 3.2]. The simple geometry of the current model demonstrates an example of how the polymer's entropy can be brought into play in modification of the membrane's surface structure.

Two other systems share some similarity in the overall theme with the current model. An interesting comparison of the current system is the droplet budding transition induced by the interfacial energy between a membrane-confined liquid droplet and a underneath, phase separated liquid [73, 66]; the interfacial energy, which plays a similar role like the line tension, is the driving force for yielding a membrane-wrapped droplet structure in a budding conformation. In another system, a polymer is sandwiched between a membrane and a hard wall which binds each other through a membrane-wall attraction; the attraction is the main factor to drive budding in this system [57, 108, 106]. In the current model, no attraction is considered, and the membrane-wall contact is realized by pressing the membrane against the wall through an external pressure. All these systems exhibit structural transitions associated with the deformable membrane surface.

We theoretically study our model by using two techniques: Monte Carlo simulation and scaling theory. The range of the reduced pressure considered in this study approximately corresponds to an external force in the range of $0.01\,nN$ to $1\,nN$ in real biological systems. As far as we are aware of, the predicted structural change described below has not been experimentally observed yet.

The discussion is organized as follows. The model is introduced in Sect. 3.2. The simulation method and results are presented in Sects. 3.3 and 3.4. In Sect. 3.5, based on the numerical results, we develop a scaling theory for the current system and compare the simulation data with the scaling predictions.

3.2 Model

As discussed in Ch. 2, the current model comprises a deformable fluid membrane pressed against a hard, flat substrate and a self-avoiding polymer sandwiched between the membrane and substrate. To keep the system simple and illustrate the important physical

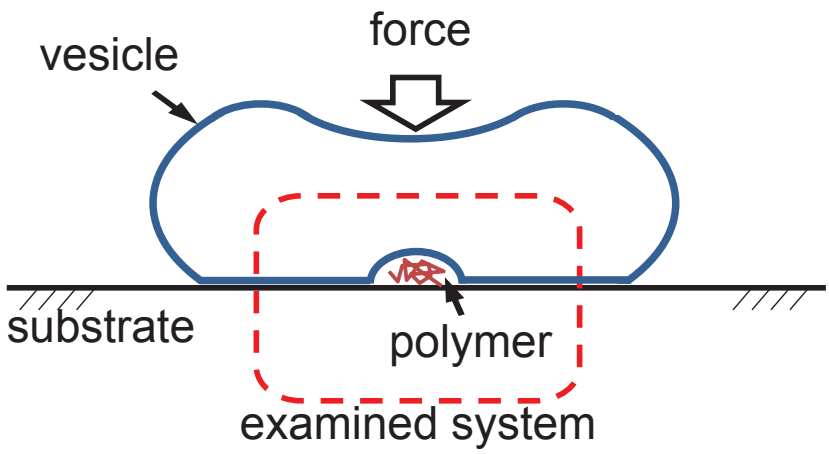

Figure 3.1: Schematic illustration of the examined system — the part inside the enclosing rectangle, which can be regarded as a part of a much larger system. A force produces the pressure needed to confine the polymer. Reprinted with permission from Ref. [107]; copyright by The American Physical Society.

properties, we only consider the excluded-volume effects between the mutually excluding monomers, between monomers and the confining walls, and between membrane and the substrate. We ignore other possible interactions in the system. The membrane is considered to be part of a much larger vesicle, which is compressed against the hard substrate under pressure p, from a force exerted on the vesicle in a direction normal to the substrate surface. A schematic illustration is shown in Fig. 3.1.

Defining V as the volume of the confining space between the membrane and the substrate, we can write the free energy of the system

$$F = F_{\text{mem}} + F_{\text{poly}} + pV, \tag{3.1}$$

where F_{mem} is the free energy difference of the membrane in reference to a state without the polymer and F_{poly} is the confinement entropy of the polymer. Although the pV term above has a similar appearance as the osmotic-pressure term in a vesicle energy model [101], the physical meaning is completely different.

Most experimentally realized membranes have a large bending modulus κ; hence, the determination of the membrane shape is dominated by the bending energy, and the thermal fluctuations are less important[100, 78]. In this study, we model the membrane's free energy

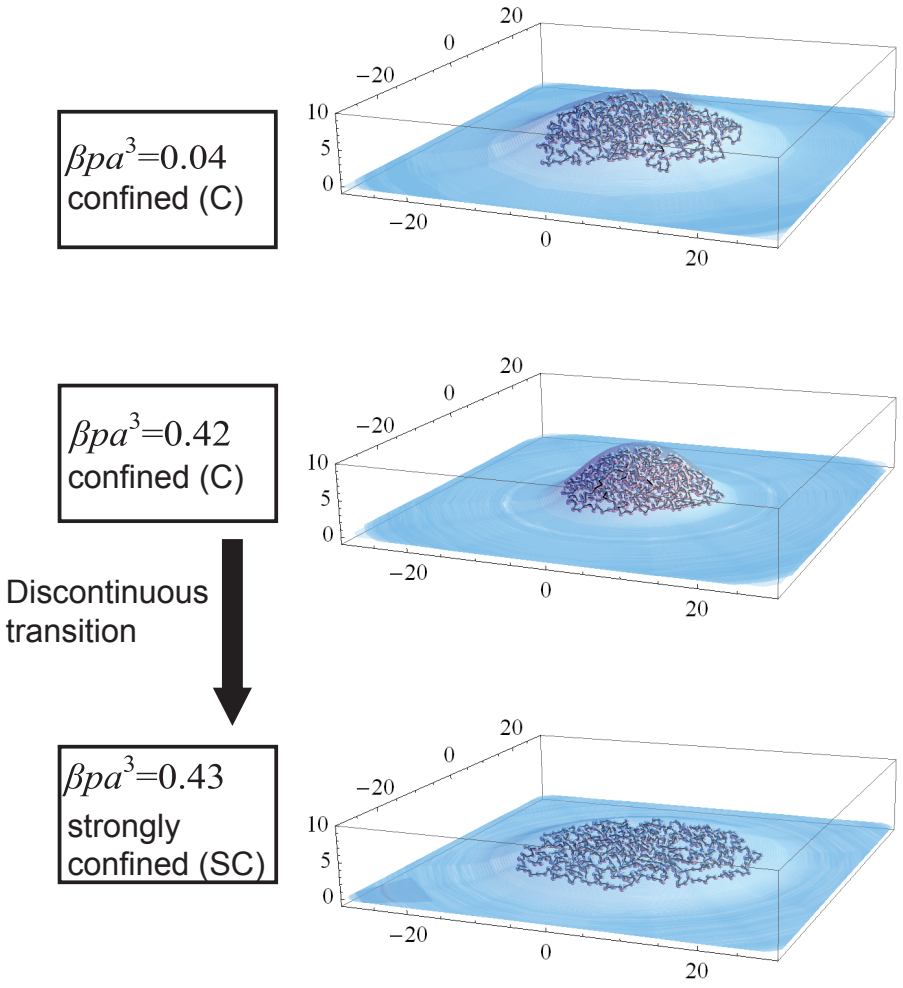

Figure 3.2: Simulation snapshots of the model system with $N = 800$ and $\beta\sigma a^2 = 0.4$. From a low pressure ($\beta pa^3 = 0.04$), the confined (C) conformation changes continuously to a more profound, localized state at the transition pressure, $\beta p^* a^3 = 0.42$. The conformation then jumps to a strongly confined (SC) state where the polymer is almost flattened out. The length scales are labeled in units of a. The size of monomers have been reduced for visualization clarity.

by the Helfrich energy [55]

$$F_{\rm mem} \simeq E_{\rm mem} = 2\kappa \int M^2 \, dA + \sigma \Delta A, \tag{3.2}$$

where M is the local mean curvature of the surface element dA. We assume that the membrane is part of a much larger, closed vesicle, in which the Gaussian curvature term is a constant not explicitly considered here. Furthermore, the requirement of the overall surface-area constraint on the original vesicle manifests into the second term in the above expression, where σ can be considered as the surface tension. Here we follow the treatment commonly used in a flat-membrane problem, taking σ as a system parameter[15, 32, 35, 36, 47], which is independent of p. The physical nature of σ, in relationship with the thermal fluctuations of the membrane constituents, is an issue that has recently been examined [45, 38]. The excess area $\Delta A = \int dA - \int' dA$ is the difference between the stretched membrane surface $\int dA$ and the projection of the area on the flat wall $\int' dA$. For simplicity, we only examine the case where the system has a zero spontaneous curvature [100, 78]. For later reference, we consider the properties of the bending energy,

$$E_b = 2\kappa \int M^2 \, dA, \tag{3.3}$$

and the surface-tension energy,

$$E_\sigma = \sigma \Delta A, \tag{3.4}$$

separately.

Within the model, an appropriate assessment of the self-avoiding polymer's entropy under strong confinement, i.e. $F_{\rm poly}$, is essential for determination of the stability of the polymer conformation. Here, we use two independent methods: a Monte Carlo simulation that automatically models the entropy (Sect. 3.3) and a scaling argument where a compression entropy can be written (Sect. 3.5).

3.3 Monte Carlo scheme

The polymer's free energy as a function of the monomer number N contains the conformational entropy and the excluded-volume interaction between the monomers. The Monte Carlo simulation is an effective tool to handle these properties efficiently.

We use a freely-rotating-chain model which contains $N-1$ bonds of bond length a. Each monomer has a hard-sphere diameter $D = 0.9a$. To update the configuration of the

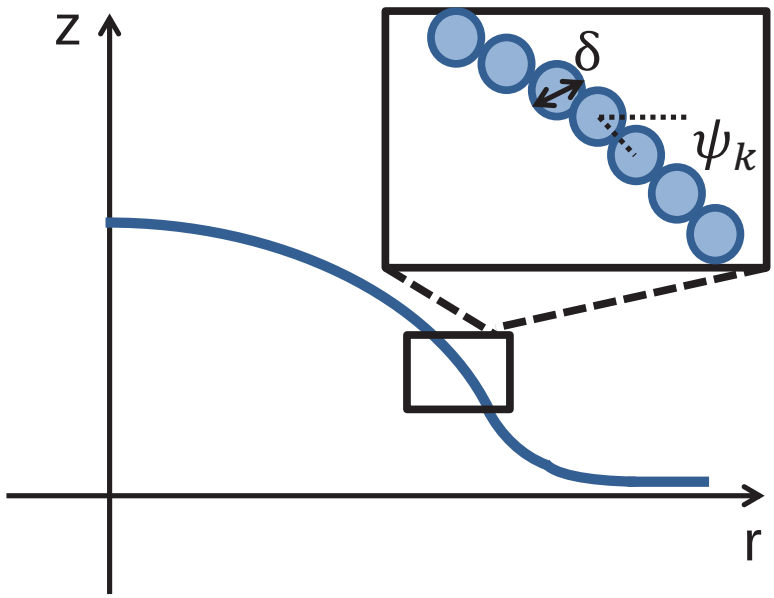

Figure 3.3: Discretization scheme of the curve describing the membrane shape. Reprinted with permission from Ref. [107]; copyright by The American Physical Society.

polymer chain, we randomly selected a monomer and rotated it about the axis formed by its adjacent monomers; the rotational angle was taken from a random selection bounded by the magnitude $|\Delta\theta|$. In order to keep the update robust, $\Delta\theta$ was adjusted to yield approximately 50% overall acceptance rate of Monte Carlo updates. The entire polymer, constrained between the membrane and the substrate surface, moves in three-dimensional space.

The structures discussed here are inherently axisymmetric; to simulate the system efficiently, the soft, deformable membrane was considered to have an axisymmetry about the z-axis in a cylindrical coordinate system. Suppression of the angular shape fluctuations is justified by the fact that at a large $\kappa = 16k_BT$, the free energy of the membrane is dominated by the bending energy and the thermal fluctuations about a minimized shape should be weak in general. In this work, we use the Monte Carlo procedure as an effective tool to attack the minimization of the system free energy, avoiding mathematical difficulties seen in solving the minimization problem of related axisymmetric membrane systems [102, 35, 36, 115, 79, 80, 31]. The procedure is not aimed at faithfully simulating the thermal fluctuations, which would require the consideration of the shape fluctuations along the

angular direction.

This axisymmetric approximation allowed us to simulate a large system which is crucial to the current model. Under this simplification, the membrane configuration can be described by a curve in a crosssection view [Fig. 3.3]. We discretized the curve into m nodes, spaced out with a distance of $\delta = a/5$ from the neighboring nodes. Rotating around the z axis, two adjacent nodes define a thin truncated cone in three dimensions. Connection of these cones form a deformable two-dimensional surface. Deformable three-dimensional membrane shapes could then be generated by changing the position of these nodes. The entire picture can be visualized as if the axisymmetric surface is divided by a series of concentric rings.

The surface is free to move, subject to the membrane energy penalty, which can be calculated from the discretized version of $E_{\rm mem}$ in Eq. (3.2). In our simulation, we employed a local "bond" fluctuation move to change the shape of the curve. Shown in Fig. 3.3, ψ_k is the angle formed by the horizontal line and the connection line between the kth and $(k+1)$th nodes. Once randomly selected, this angle is adjusted by a small random number. Such a local move has a nonlocal effect: the coordinates of nodes having a label $i > k$ are all affected. In addition, to avoid the penetration of the last node into the hard-wall interior (or detachment from the wall, depending on the sign of the random number), a global translation move was considered along the z direction, to ensure that the last node of the membrane is in contact with the wall surface.

The confinement of the polymer by the soft membrane was effectively modeled by assuming that each membrane node has a hard-core diameter $\delta = a/5$. The excluded-volume interaction between these membrane nodes and polymer monomers prevents mutual crossing of the two. Beyond the excluded-volume requirement, the acceptance of a move was evaluated based on the statistical weight $\exp[-\beta(E_{\rm mem} + pV)]$, according to the Metropolis algorithm. The reduced bending modulus, $\beta\kappa$, was fixed at 16, corresponding to the order of magnitude in actual biological systems [100, 78]. In this formalism, $\beta = 1/k_BT$, where k_B is the Boltzmann constant and T the room temperature. Examining the entire model in reduced units, we can show that the system is controlled completely by three independent parameters: N, $\beta\sigma a^2$, and $\beta p a^3$.

As a final technical note, we define a Monte Carlo step such that it consists of N attempts of moving a randomly selected monomer and $m/10$ attempts of changing the positions of randomly selected membrane nodes. A typical data point corresponding to a given set of N, $\beta\sigma a^2$, and $\beta p a^3$ was averaged over the accumulated data from 3×10^6 Monte Carlo steps. An equal number of steps were used for the initial equilibration.

In our Monte Carlo simulation, we considered the reduced-pressure range, $\beta p a^3$, from

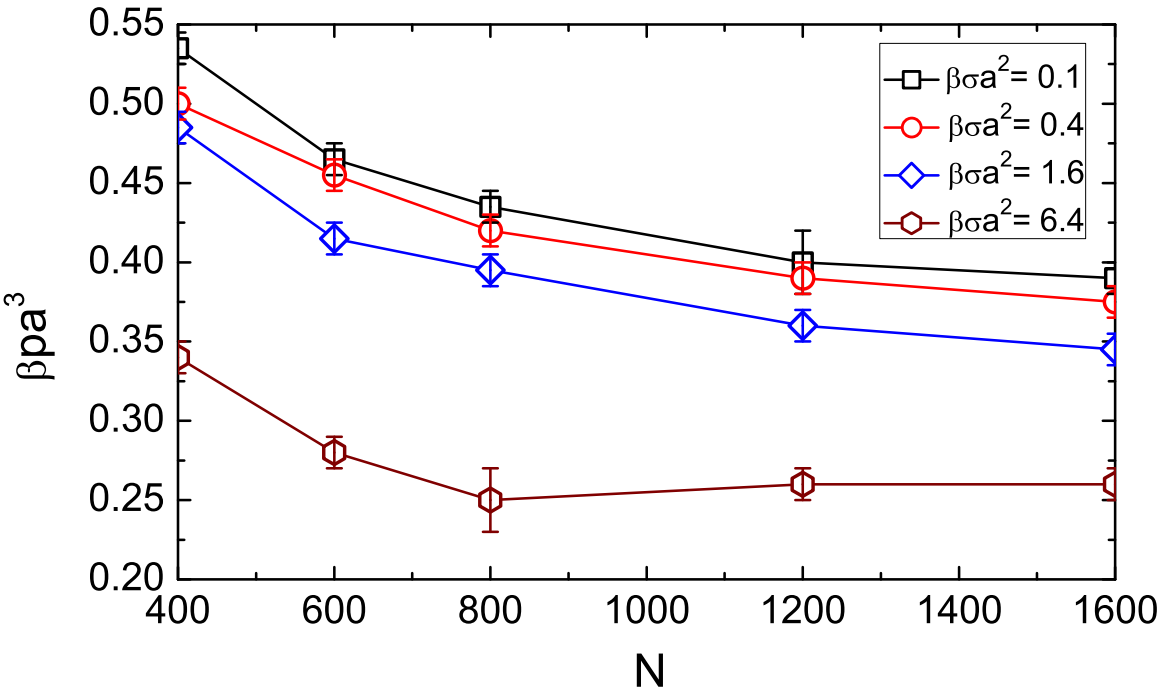

Figure 3.4: Phase boundaries between the strongly confined state (up right region) and the confined state (low left region) for various values of $\beta\sigma a^2$. Symbols are the transition points determined by the Monte Carlo simulation, and lines are the estimated boundary. A first-order transition occurs when the system crosses the boundary line. Reprinted with permission from Ref. [107]; copyright by The American Physical Society.

0.01 to 3.0. To estimate the real pressure values in the laboratory, for example, take a typical value $a = 50\,nm$, we can estimate that p is in the range of $10^{-4}\,atm$ to $10^{-2}\,atm$. If we further assume that the pressure is produced by exerting a force on the vesicle, as illustrated in Fig. 3.1, and that the contact area between the vesicle and the substrate is approximately $1\,\mu m^2$, the pressure range corresponds to a force range from $0.01\,nN$ to $1\,nN$, which is realizable in a laboratory.

3.4 Numerical results and discussion

Now we present the results from the Monte Carlo study. At a large N, a discontinuous transition is observed in our simulation when we fix N and adjust βpa^3. At low βpa^3, the system is in a confined (C) state where the polymer dimensions in the vertical and horizontal directions are comparable and the monomer density is low. At high βpa^3, a strongly confined (SC) state is observed, where the polymer is completely compressed on the substrate surface, and the monomer density is relatively high. The lines in Fig. 3.4 show the C-SC phase boundaries for various values of $\beta\sigma a^2$; one of the outstanding features is that either a larger $\beta\sigma a^2$ or a larger N prefers a lower transition pressure.

The measurements for various components of the membrane energy at $\beta\sigma a^2 = 0.1$ and $\beta\sigma a^2 = 6.4$ are plotted in Fig. 3.5(a). The bending energy E_b and the surface tension energy E_σ decrease after the C-SC transition. Before the C-SC transition, in the C state, the confinement volume, $\langle V\rangle/a^3$, decreases steadily as the pressure increases, as shown in Fig. 3.5(b). Across the transition point, however, both $\langle V\rangle/a^3$ and $p\langle V\rangle$ [diamonds in Fig. 3.5(a)] jump to a higher value in the SC state, after which $\langle V\rangle/a^3$ regains the declining course when βpa^3 further increases. This jump is somewhat counter-intuitive. One of the main effects of an increasing pressure is driving the confinement volume to a smaller size; as such the mean curvature wrapping around a smaller volume increases. The bending energy, as well as the surface-tension energy associated with a excess surface area, prefers the SC state, where the shape curve is more smooth and the excess surface area is at its minimum. In other words, the C-SC transition is pressure driven, but the important benefactor is the membrane's energy, not the work term, pV.

The open and filled symbols in Fig. 3.5 are for two different values of $\beta\sigma a^2$. The energy gap at the C-SC transition shrinks as $\beta\sigma a^2$ increases. A large $\beta\sigma a^2$ leads to a more rigid membrane; thus, the membrane deformation becomes less significant across the transition, which yields a subtle shape difference between the C and SC states. Within the current Monte Carlo data, we cannot resolve whether these two states would merge and the C-SC transition would disappear at a much larger $\beta\sigma a^2$ than the range observed here.

To understand the conformation of the confined polymer, two ratios of the polymer dimensions, ξ_z and ξ_{xy}, were measured in the simulation,

$$\xi_z \equiv \langle S_z^2\rangle/\langle S_{z,0}^2\rangle, \tag{3.5}$$

and

$$\xi_{xy} \equiv \langle S_{xy}^2\rangle/\langle S_{xy,0}^2\rangle, \tag{3.6}$$

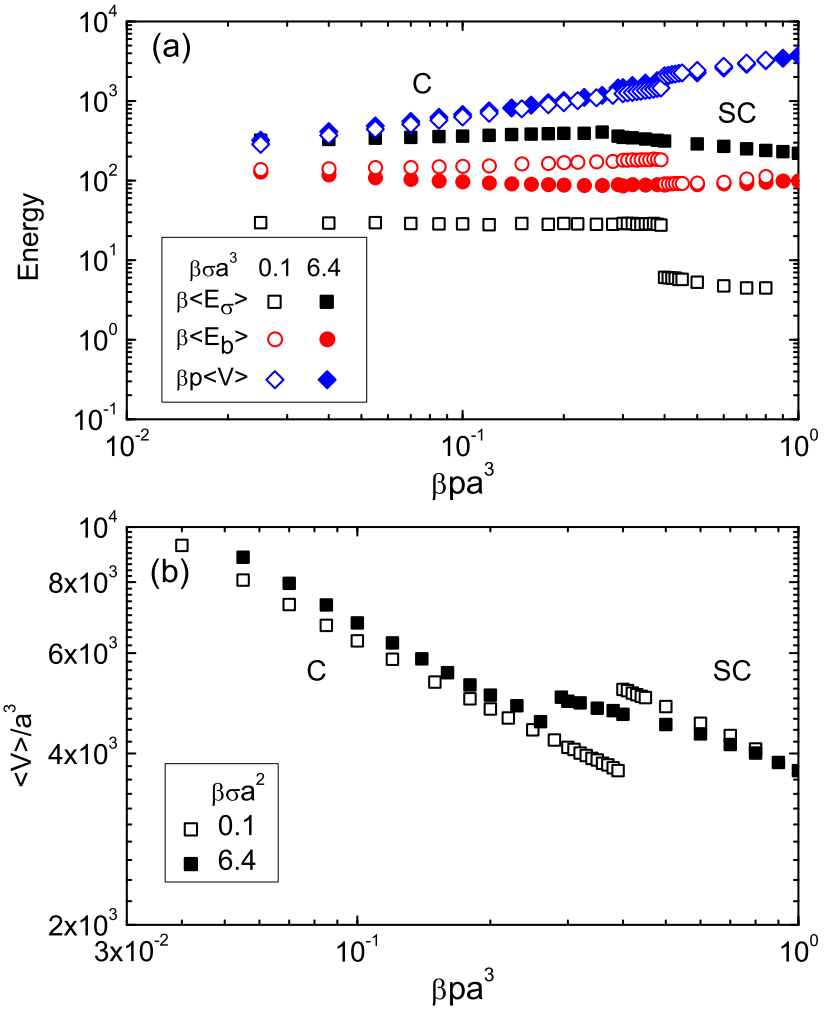

Figure 3.5: Monte Carlo simulation data with $N = 1600$ as a function of $\beta p a^3$ for $\beta\sigma a^2 = 0.1$ (open symbols) and $\beta\sigma a^2 = 6.4$ (filled symbols): (a) the energy components in the system. Increasing the surface tension, $\beta\sigma a^2$, minimizes the energy gap between the states. (b) The system volume, $\langle V\rangle/a^3$, increases after the jump from the confined state to the strongly confined state. The estimated error bars are smaller than the size of the symbols plotted in (a) and (b). Reprinted with permission from Ref. [107]; copyright by The American Physical Society.

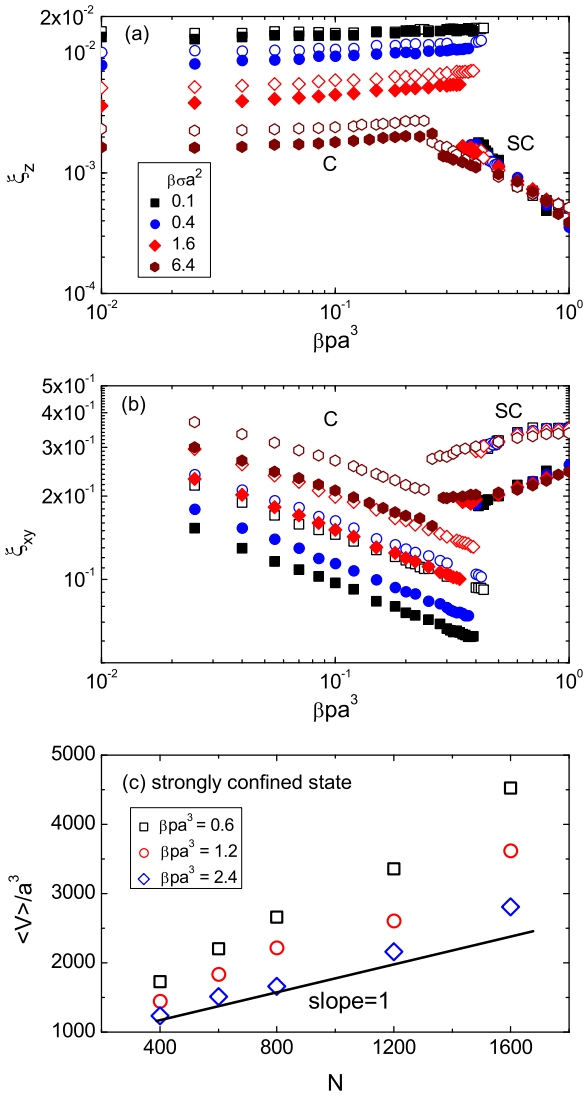

Figure 3.6: Ratios of the polymer's gyration dimensions along (a) the z-axis and (b) in xy-plane, defined in Eqs. (3.5) and (3.6). All filled symbols correspond to $N = 1600$ and open symbols correspond to $N = 800$. (c) The system volume as a function of N at $\beta\sigma a^2 = 0.4$ for various βpa^3. As the pressure rises, V becomes proportional to N. In (a), (b), and (c), the estimated error bars are smaller than the size of the symbols plotted. Reprinted with permission from Ref. [107]; copyright by The American Physical Society.

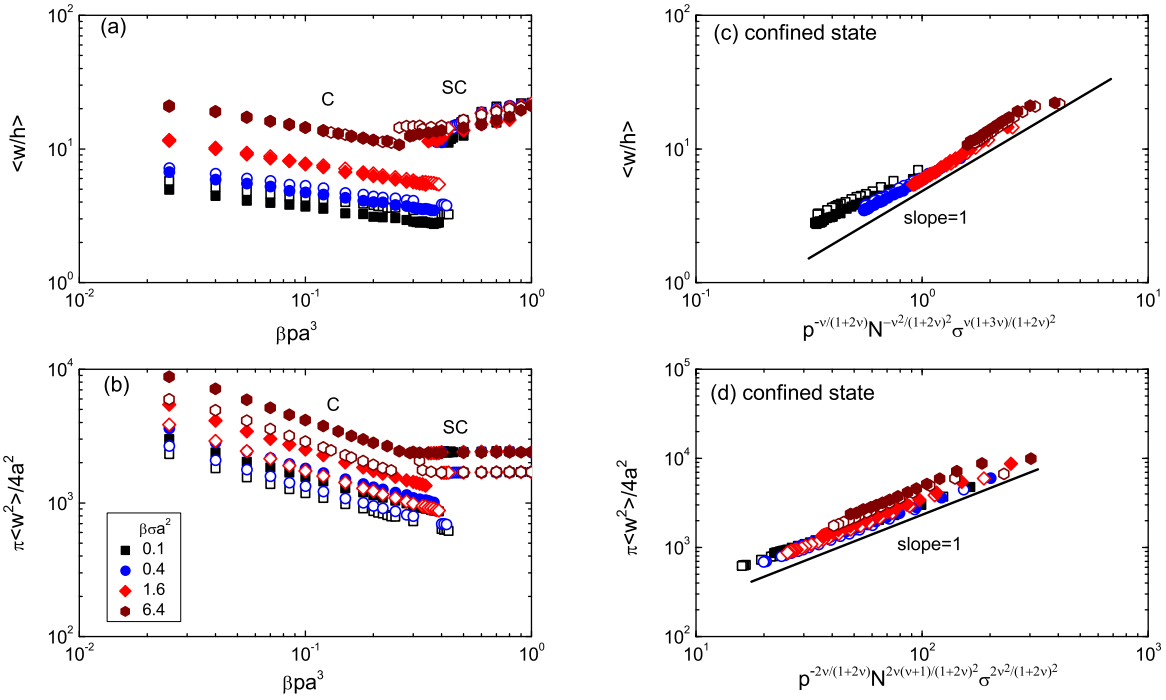

Figure 3.7: (a) The aspect ratio, $\langle w/h \rangle$, and (b) the open surface area not in contact with the membrane, $\pi \langle w^2 \rangle / 4a^2$, measured from the Monte Carlo simulation, as functions of $\beta p a^3$ for $N = 1600$ (filled symbols), $N = 800$ (open symbols) and various $\beta \sigma a^2$ specified in (b). To compare the simulation data with the scaling prediction in the confined state, the horizontal axes in (c) and (d) are rescaled according to Eqs. (3.12) and (3.13); factors of β and a are set to 1 in these plots for simplicity. The estimated error bars are smaller than the size of the symbols plotted in all figures. Reprinted with permission from Ref. [107]; copyright by The American Physical Society.

where $\langle S_{xy}^2 \rangle$ and $\langle S_z^2 \rangle$ are the mean square radii of gyration measured in the xy-plane and along the z-axis respectively, and $\langle S_{xy,0}^2 \rangle$ and $\langle S_{z,0}^2 \rangle$ the counterparts of a free polymer. These are shown in Figs. 3.6(a) and (b). Crossing the C-SC transition, the overall polymer conformation undergoes a transition from a half globular shape to a compressed, almost two-dimensional shape against the wall at a high pressure. We can also demonstrate this conformational transition by examining the aspect ratio, w/h, displayed in Fig. 3.7(a), where h is the height of the membrane at the symmetry axis and w the diameter of the detached portion of the membrane from the flat wall. Further increase of $\beta p a^3$ in the SC state suppresses the z-direction polymer fluctuations, but would not yield further expansion of the confinement cavity along the surface direction; the latter is shown by a constant behavior of $\pi w^2/4a^2$ after the C-SC transition, displayed in Fig. 3.7(b).

3.5 Scaling discussion

Some of the observed properties in the above section can be made explicit in a scaling argument. In the confined (C) state the monomer density is relatively low; we can write down the entropy of the confined polymer and explain the observed physical properties quantitatively. In the strongly confined (SC) state the monomer density is relatively high hence the scaling argument of the polymer entropy fails; however, the qualitative behavior of the phase diagram can still be discussed.

In the C state, changes in the reduced pressure $\beta p a^3$ or surface tension $\beta \sigma a^2$ influence both polymer dimensions ξ_z and ξ_{xy}. This indicates that the confinement entropy of the polymer in both lateral and vertical directions need to be taken into account in a scaling theory. According to Ref. [33] and Sect. 2.3, the compression entropy in these directions can be separately written as $N\big(a/h\big)^{\frac{1}{\nu}}$ and $N\big(a/w\big)^{\frac{1}{\nu}}$. For the current purpose we assume that a sum can be taken,

$$\beta F_{\rm poly} \sim N\big[\big(\frac{a}{h}\big)^{\frac{1}{\nu}} + \big(\frac{a}{w}\big)^{\frac{1}{\nu}}\big], \tag{3.7}$$

where numerical coefficients have been dropped.

The analysis of the membrane energy can be made by approximating the shape of the confining membrane portion. Using a spherical cap of a base area $4\pi w^2$ and height h, we arrive at the scaling form for the two terms in Eq. (3.2),

$$\beta E_{\rm mem} \sim \beta\kappa \frac{h^2}{w^2} + \beta\sigma h^2. \tag{3.8}$$

Finally, taking into account the fact that volume V can be calculated from w^2h, we can write the free energy for the system in a C state,

$$\beta F_C \sim \beta\kappa\frac{h^2}{w^2} + \beta\sigma h^2 + N\left[\left(\frac{a}{h}\right)^{\frac{1}{\nu}} + \left(\frac{a}{w}\right)^{\frac{1}{\nu}}\right] + \beta p w^2 h, \tag{3.9}$$

which is a function of variables h and w.

In most parameter region for the C state, $w/a \gg 1$ and $\kappa \ll \sigma w^2$; therefore, we can safely discard the first term. Then, minimizing the total free energy with respect to w and h gives,

$$\beta p w h - N\frac{a^{\frac{1}{\nu}}}{w^{\frac{1+\nu}{\nu}}} = 0; \tag{3.10}$$

$$\beta\sigma h + \beta p w^2 - N\frac{a^{\frac{1}{\nu}}}{h^{\frac{1+\nu}{\nu}}} = 0. \tag{3.11}$$

Comparing the magnitude of the σ- and p-related terms in the second equation in reference to the range of parameters considered in the Monte Carlo simulation, we can show that the σ-related term dominates over the p-related term in the weak pressure region. This is also supported by the simulation data shown in Fig. 3.5(a) where the C branch of $\beta\langle E_\sigma\rangle$ remains almost constant. Neglecting the p-related term in Eq. (3.11) but keeping it in Eq. (3.10), we can solve for w and h,

$$w \sim p^{\frac{-\nu}{1+2\nu}}\sigma^{\frac{\nu^2}{(1+2\nu)^2}}N^{\frac{\nu(\nu+1)}{(1+2\nu)^2}}, \tag{3.12}$$

and

$$\frac{w}{h} \sim p^{\frac{-\nu}{1+2\nu}}\sigma^{\frac{\nu(1+3\nu)}{(1+2\nu)^2}}N^{\frac{-\nu^2}{(1+2\nu)^2}}. \tag{3.13}$$

The solid lines in log-log plots in Figs. 3.7(c) and (d) demonstrate these power laws, after the substitution of the Flory exponent $\nu = 3/5$. Our simulation results in Figs. 3.7(a) and (b), represented by symbols, collapse on the scaling prediction laws in Figs. 3.7(c) and (d).

In the SC state, the polymer is flattened out to form mono- or double monomer layers, regardless of the value of $\beta\sigma a^2$ and N. In some of the high $\beta p a^3$ systems simulated here, we can estimate that the monomer density inside the confinement volume becomes comparable to (but still much less than) the close packing density. In the latter case, $\langle V\rangle/a^3$ should be proportional to the monomer numbers N, as indicated by the solid line in Fig. 3.6(c). Because of the relatively high monomer density, the polymer entropy can no longer be estimated by the scaling form, Eq. (3.7). We are unable to deduce any further quantitative scaling relations for the SC state.

In the SC state, according to Fig. 3.5(a), the free energy is dominated by the pV term,

$$F_{\mathrm{SC}} \sim pV. \tag{3.14}$$

Furthermore, for a qualitative purpose we assume

$$V \sim N^{\alpha}, \tag{3.15}$$

where $\alpha = 1$ is characteristic of the close-packing limit that the monomer density cannot exceed. Combining these we obtain,

$$F_{\mathrm{SC}} \sim pN^{\alpha}. \tag{3.16}$$

On the other hand, plugging Eqs. (3.12) and (3.13) into Eq. (3.9) and keeping the leading term we have the free energy for the C state in a scaling form,

$$F_C \sim p^{\frac{1}{1+2\nu}} \sigma^{\frac{-\nu}{(1+2\nu)^2}} N^{1-\frac{\nu+1}{(1+2\nu)^2}}. \tag{3.17}$$

To unravel the general behavior of the transition pressure p^*, we equate Eq. (3.16) with Eq. (3.17). The transition pressure can then be estimated,

$$p^* \sim \sigma^{\frac{-1}{2(1+2\nu)}} N^{\frac{1+2\nu}{2\nu}\left(1-\frac{\nu+1}{(1+2\nu)^2}-\alpha\right)}. \tag{3.18}$$

The exponent of N is negative because $\alpha(p) \sim 1$. Hence we see that increasing either σ or N lower the transition pressure p^*, which is a qualitative behavior in agreement with the phase diagram presented in Fig. 3.4.

3.6 Summary

In this study, the model of a self-avoiding polymer pressed by a soft membrane on one side and confined by a hard surface on the other side was studied. Using the Monte Carlo simulation, we demonstrated that, at large monomer numbers, this simple system displays a discontinuous transition from the confined state to the strongly confined state. The properties of each state were discussed. We showed that in the confined state increasing the pressure helps to reduce the non-contact area between the membrane and the substrate; going through the confined to strongly confined transition by increasing pressure, the non-contact area, however, jumps to a large value. A scaling argument was also developed and agrees with the Monte Carlo data in the confined state.

We hope that the study of this simple system can improve the current understanding of the role played by pressure in a polymer-membrane complex and stimulates experimentalists to develop tools to probe the mechanical properties of this system. A possible experimental realization of the current model is using the micropipette technique to hold and push a cell against a substrate sparsely grafted with polymers, which can be done rather straightforwardly [86, 27, 26].

The current chapter and the previous chapter concern about the conformational properties of a single polymer, in two different scenarios of confinement by a soft membrane against a hard wall. The physical setup of the system bears similarity to a polymer confined near a hard wall by a low molecular film [54]. In the latter system, Halperin *et al.* have predicted that multiple confined polymers can undergo a phase separation on the quasi two-dimensional surface. The complication of confining multiple polymers in the current model, i.e. the possibility of phase separation on the surface, requires further exploration.

Chapter 4

Model of vesicle tubulation and pearling induced by nanoparticles

4.1 Introduction

In recent years, self-assembly of nanoparticles adsorbed on lipid bilayer membranes has been studied extensively due to its interestingly rich phenomenon [97]. Nanoparticles having different shapes and adhesion strength to membranes are possible to create different structures of protrusions. For example, one single spherical particle with strong adhesion energy is wrapped completely by a membrane and forms a bud [71, 84, 36, 53, 68, 118, 21, 112]. Furthermore, with multiple spherical nanopartiles and proper adehsion strength, it is also possible to form a tubular structure that the diameter of the tube is exactly the diameter of nanoparticles [96, 6]. On the other hand, multiple spherical caps are able to produce a tubular structure that the diameter of the tube is larger than the size of the cap [92]. Apparently, the shapes of the protrusions depend on the balance between the nanoparticle adhesion strength and the deformation capability. However, each of these results represents a particular combination of these factors; relatively little is known about how these factors generates various structures of the protrusions in general.

In this chapter, we propose a grand canonical model and present its solution to address the above question. By decoupling the nanoparticle adhesion strength from its deformation capability, which is physically quantified by the spontaneous curvature, structure diagrams were computed and various structures were found. We begin by discussing the proposed model and the numerical scheme. Then the results obtained by minimizing the free energy

numerically are discussed, which we focus on the pearling structures that are in accordance with a recent experiment [119].

4.2 Theory

To study the main physical mechanism of tubulation and pearling induced by nanoparticles, we consider an vesicle in contact with a nanoparticle solution inside and outside of it. For simplicity we assume there is no interaction between nanoparticles themselves and they can be adsorbed onto the membrane surface. Then, the total free energy $F_{\rm tot}$ is the sum of the bending energy, $F_{\rm mem}$, and the free energy $F_{\rm ad}$ contributed by nanoparticle adsorption:

$$F_{\rm tot} = F_{\rm mem} + F_{\rm ad}. \tag{4.1}$$

One of the major effects of the adsorption of nanoparticles is that it causes an asymmetric configuration between the two leaflets of the membrane. The adsorbed site on the membrane tends to deform locally and generate a spontaneous curvature [119]. To proceed further, we introduce $\phi(\mathbf{x})$ as the difference of the area fraction of the inner and outer surfaces that are affected by nanoparticle adsorption, where $\mathbf{x}$ is the coordinate of a surface element. Phenomenologically, we assume that the local spontaneous curvature is linearly coupled to $\phi(\mathbf{x})$ by a curvature constant c_0; a similar assumption has been proposed to study the effect of the polymer anchoring on membranes [18]. We can then write down the modified Canham-Helfrich energy [20, 55] as

$$F_{\rm mem} = \frac{\kappa}{2} \int \left[2M - c_0\phi(\boldsymbol{x})\right]^2 dA, \tag{4.2}$$

where M is the mean curvature of the surface area element dA, and κ is the bending modulus.

The nanoparticle solution provides a reservoir for nanoparticles that are adsorbed on the membrane surface. On the basis of the grand canonical ensemble, we can simply assume that

$$F_{\rm ad} = \mu_0 n, \tag{4.3}$$

where the negative μ_0 is the free energy loss of a nanoparticle in the adsorbed state, which is coupled with the adhesion strength, and n is the total number difference of the adsorbed nanoparticles between the inner and outer surfaces. Using the definition of $\phi(\mathbf{x})$,

we can readily write $n = \int \phi(\mathbf{x})\, dA/A_\mathrm{p}$, where A_p is the effective contact surface area of a nanoparticle with the membrane. Hence, the adsorption energy can be written as

$$F_\mathrm{ad} = \mu \int \phi(\mathbf{x})\, dA \tag{4.4}$$

where $\mu \equiv \mu_0/A_\mathrm{p}$ is a renormalized adsorption parameter.

In summary, with a vesicle under the constraint of constant area A and volume V, this simple model is controlled by four parameters: the bending modulus κ, the spontaneous curvature c_0, the chemical potential μ, and the reduced volume v. The reduced volume v is defined as

$$v = \frac{V}{(4\pi/3)R_s^3}, \tag{4.5}$$

where

$$R_s = (A/4\pi)^{1/2}. \tag{4.6}$$

The total free energy F_tot in Eq. 4.1 can be transformed into a dimensionless function:

$$F_\mathrm{tot}/\kappa = \frac{1}{2}\int \left[2MR_s - \tilde{c}_0\phi(\boldsymbol{x})\right]^2 d\tilde{A} + \tilde{\mu}\int \phi\, d\tilde{A}, \tag{4.7}$$

where $\tilde{c}_0$ is the reduced spontaneous curvature $\tilde{c}_0 = c_0 R_s$ and $\tilde{\mu}$ is the reduced chemical potential $\tilde{\mu} = \mu R_s^2/\kappa$. The area element is reduced to $d\tilde{A} = dA/R_s^2$.

4.3 Numerical scheme

The difficulties of studying the described model arise from the fact that the shape of the membrane surface and the area fraction $\phi(\boldsymbol{x})$ change simultaneously. In previous studies where similar models were dealt with [52, 18, 19, 60], the membrane shape was derived according to the assumption that the area fraction $\phi(\boldsymbol{x})$ has a predetermined function form. In this section, we introduce a minimization framework that allows both the membrane shape and the area fraction $\phi(\boldsymbol{x})$ to vary without any assumption about their values.

We consider a vesicle with a deformable surface that has an axisymmetry about the z axis. The shape of the vesicle can be described completely by a curve with coordinates $r(s)$ and $z(s)$, where r is the radial variable and s is the arclength along the contour. In our numerical procedure, the curve is discretized into N nodes, each separated by a distance d.

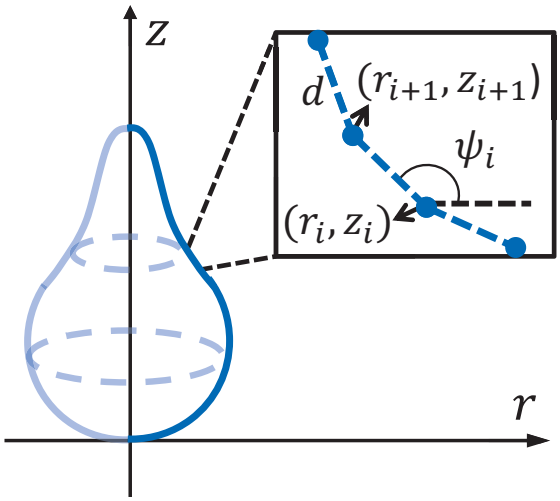

Figure 4.1: Discretization scheme of the shape curve representing the vesicle in an axisymmetric setting. The curve is discretized into N nodes by a distance d. Variables r_k and ψ_k $(k = 1, 2, ..., N)$ were treated as independent variables in our minimization scheme.

We further introduce an angle variable ψ, which is defined as the angle between the nodes and the horizontal line. The coordinates r and z depend on ψ through

$$r_{i+1} = r_i + d\cos\psi_i, \tag{4.8}$$
$$z_{i+1} = z_i + d\sin\psi_i, \tag{4.9}$$

where i is the index number of nodes. This discretization scheme is illustrated in Fig. 4.1.

With axisymmetry the adsorption of nanoparticles onto the membrane surface is described by the area fraction $\phi(s)$ as a function of the arclength s. We also discretize $\phi(s)$ into ϕ_i for every node i with the constraint $0 \leq \phi_k \leq 1$. Since later we will minimize the total free energy F_{tot} to find the optimal distribution of the area fraction ϕ, no constraint is placed on the total amount of area occupied by adsorbed nanoparticles.

To minimize the total free energy F_{tot}, within the axisymmetry scheme, we introduce

a dimensionless target function with a discretized form of Eq. (4.7):

$$\begin{aligned}\tilde{F} =& \frac{1}{2}\sum_i \big[\frac{\psi_{i+1}-\psi_i}{\tilde{d}} + \frac{\sin\psi_i}{\tilde{r}_i} - \tilde{c}_0\phi_i\big]^2 \Delta\tilde{A}_i \\ &+ \tilde{\mu}\sum_i \phi_i \Delta\tilde{A}_i \\ &+ \Lambda_A\big(1 - \frac{1}{4\pi}\sum_i \Delta\tilde{A}_i\big)^2 \\ &+ \Lambda_V\big(1 - \frac{3}{4v}\sum_i \big(\frac{\tilde{r}_{i+1}+\tilde{r}_i}{2}\big)^2 \tilde{d}\sin\psi_i\big)^2 \\ &+ \Lambda_d \sum_i (\tilde{r}_{i+1} - \tilde{r}_i - \tilde{d}\cos\psi_i)^2,\end{aligned} \tag{4.10}$$

where $\Delta\tilde{A}_i = \pi\tilde{d}(\tilde{r}_{i+1}+\tilde{r}_i)$ with $\tilde{d} = d/R_s$ and $\tilde{r}_i = r_i/R_s$. The Λ_A and Λ_V terms constrain the area and volume according to the reduced volume v, and the Λ_d term is added because $\tilde{r}_i$, ψ_i, ϕ_i and $\tilde{d}$ are treated as independent variables in our minimization scheme. The model under consideration is controlled completely by the dimensionless parameters $\tilde{c}_0$, $\tilde{\mu}$ and v.

We minimized the above target function with $N = 301$ using L-BFGS-B algorithm [17] iteratively. Each time the penalty factors Λ_A, Λ_V, Λ_d were increased by 1 percent starting from 500 to 10^7. The error tolerance of the minimization was selected such that the contribution of the penalty terms was less than 0.1 percent to the final minimized target function value.

4.4 Results and discussion

In our simulation, we explored the $\tilde{\mu} < 0$ region, which the imbalance of nanoparticles between the inner and outer surfaces is favored. This mechanism was proposed to explain the experimental results [119]; If the inner and outer surfaces were balanced initially, there would be no protrusion, and the system becomes a simple vesicle without spontaneous curvature studied in Ref. [101].

Instead of plotting all the configurations obtained by minimization, and to understand the overall structure of the model, we defined a shape parameter γ to measure how well the beads are formed in the protrusion part:

$$\gamma = \frac{\tilde{r}_{\text{avg}} - (1/\tilde{c}_0)}{\pi/(2\tilde{c}_0) - (1/\tilde{c}_0)}, \tag{4.11}$$

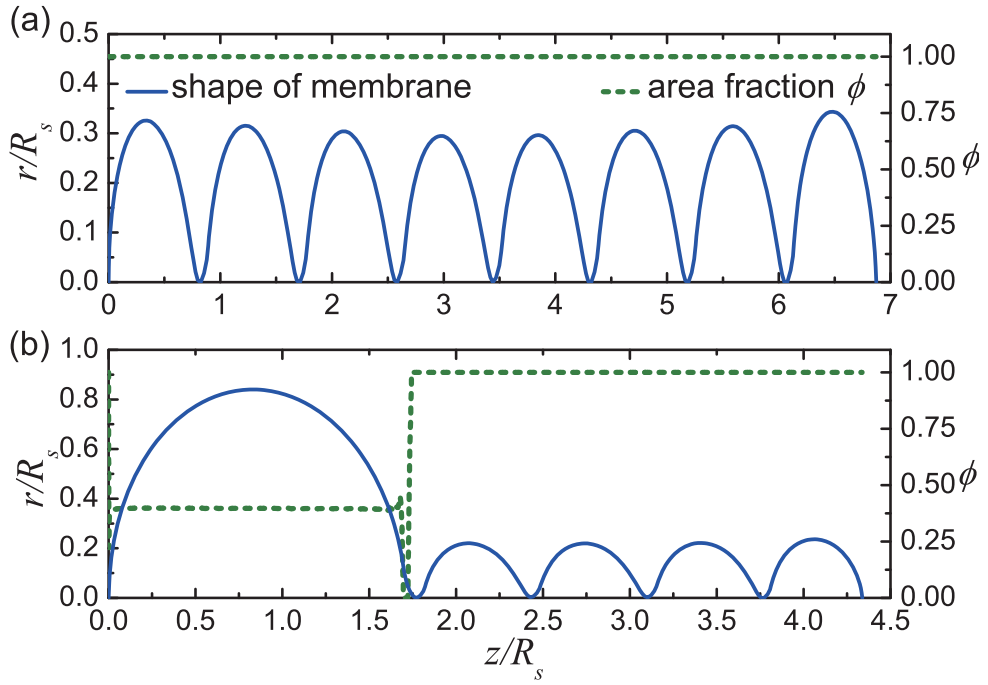

Figure 4.2: The shape of pearling structures (solid line) and the area fraction ϕ (dashed line). (a) $\tilde{c}_0 = 5.0$, $\tilde{\mu} = -3.56$ and $v = 0.35$. (b) $\tilde{c}_0 = 7.6$, $\tilde{\mu} = -0.51$ and $v = 0.70$; The configuration comprises two states: one is the pearling part ($\phi = 1.0$), and the mother vesicle is an almost perfect sphere that can be regarded as an reservoir to adjust the area and volume of the vesicle. Note that the axes of r and z are not in the same scale.

where $\tilde{r}_{\rm avg} = R_s^{-1} \int_p r(x)\, dA / \int_p dA$, and $\int_p dA$ is the the area of the protrusion part. If the protrusion forms a tube with a radius equal to $1/\tilde{c}_0$, then $r_{\rm avg} = 1/\tilde{c}_0$. On the other hand, if it forms a string of beads with a radius equal to $2/\tilde{c}_0$, then $r_{\rm avg} = \pi/(2\tilde{c}_0)$. Thus the numerical parameter γ indicates the shape of the protrusion: $\gamma \simeq 1$ means the shape resembles beads and $\gamma \simeq 0$ means the shape resembles a tube.

4.4.1 Properties of stable states

We begin our discussion of the numerical results by examining how the vesicle shape intertwines with the distribution of the area fraction adsorbed by nanoparticles. In Fig. 4.2, the vesicle shapes and the distribution of spontaneous curvature are determined through

interacting with each other. In contrast, previous studies obtained a similar morphology by assuming a uniform distribution of spontaneous curvature [52, 18]. The results we found here explain why this is the case; the area fraction ϕ equals to 1.0 throughout the pearling part. Note that the radius of the pearling structure is close to $2/\tilde{c}_0$. This implies we may use the observed bead size in the experiment to estimate the spontaneous curvature generated by the nanoparticles.

Fig. 4.2(a) demonstrates a consistent simulation result with the experiment that Yu and Granick reported no evident accumulation of nanoparticles at regions with a specific curvature when the whole vesicle transforms into a string of beads [119]. Moreover, in Fig. 4.2(b), near the neck connecting the protrusion and the mother vesicle, the area fraction ϕ has a strong decreasing gradient, and ϕ drops to 0 at the neck, which implies the mean curvature of the membrane is zero at the neck. The mother vesicle in Fig. 4.2(b) forms an almost perfect sphere, and the area fraction ϕ is distributed uniformly. The value of ϕ of the mother vesicle agrees well with the estimation obtained from which a spherical vesicle with the known radius is fed into Eq. 4.7 to perform minimization with respect to ϕ. We shall see in the following discussion that the mother vesicle serves as an reservoir for the protrusion part to adjust the area and volume of the vesicle.

4.4.2 Properties in $(\tilde{c}_0, v)$ plane

Since the reduced spontaneous curvature $\tilde{c}_0$ controls the shapes of protrusion, which has a specific area and a specific volume, and the whole vesicle is constrained by the reduced volume v, the shapes of the vesicle should depend strongly on the the relative size of $\tilde{c}_0$ and v. In Fig. 4.3, using the shape parameter γ, we plotted the phase diagram in the $(\tilde{c}_0, v)$ plane. The band structures appeared in the figure implies the above argument is indeed true. The shapes of the vesicles in each band from blue, white to red (or yellow) possess a particular number of beads. Starting from the top left corner of the figure is one bead, and moving through each band increases the number of beads by one. Examples can be seen from the shapes plotted in Fig. 4.3. In addition, when $v \lesssim 3.0$, the vesicle adopts the shape of a long narrow capped cylinder. Likewise, when $\tilde{c}_0 \gtrsim 10$, the protrusion tends to form a tubular structure. We will discuss these two features in the following discussion.

For varying the reduced volume v, it can be regarded as fixing the area and changing the volume of the vesicle. This process resembles what have been observed in the experiment. In Fig. 4.4(a), the free energy F_{tot} decreases as v decreases. Decreasing v allows more membrane to adopt a shape according to the reduced spontaneous curvature $\tilde{c}_0$, so $\int \phi(x)\, dA$ increases, which means that the imbalance between the two surfaces increases

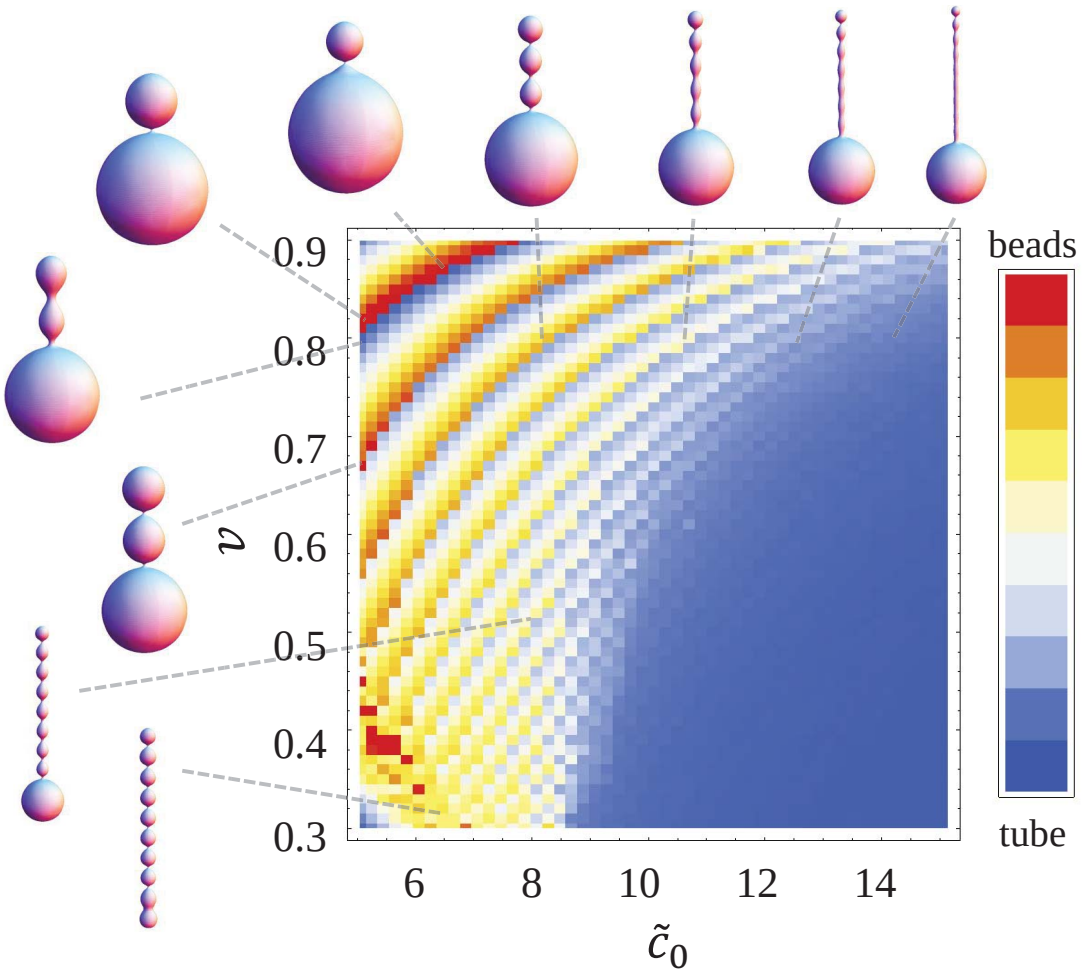

Figure 4.3: Phase diagram of the reduced volume v versus the reduced spontaneous curvature $\tilde{c}_0$ for the reduced chemical potential $\tilde{\mu} = -5.1$. The diagram is plotted using the shape parameter γ in Eq. 4.11, where the red color ($\gamma \simeq 1$) represents the membrane forms one or several perfect beads and the blue color ($\gamma \simeq 0$) represents a perfect tubular protrusion structure. Each band from blue, white to red (or yellow) has a particular number of beads in the protrusion structure.

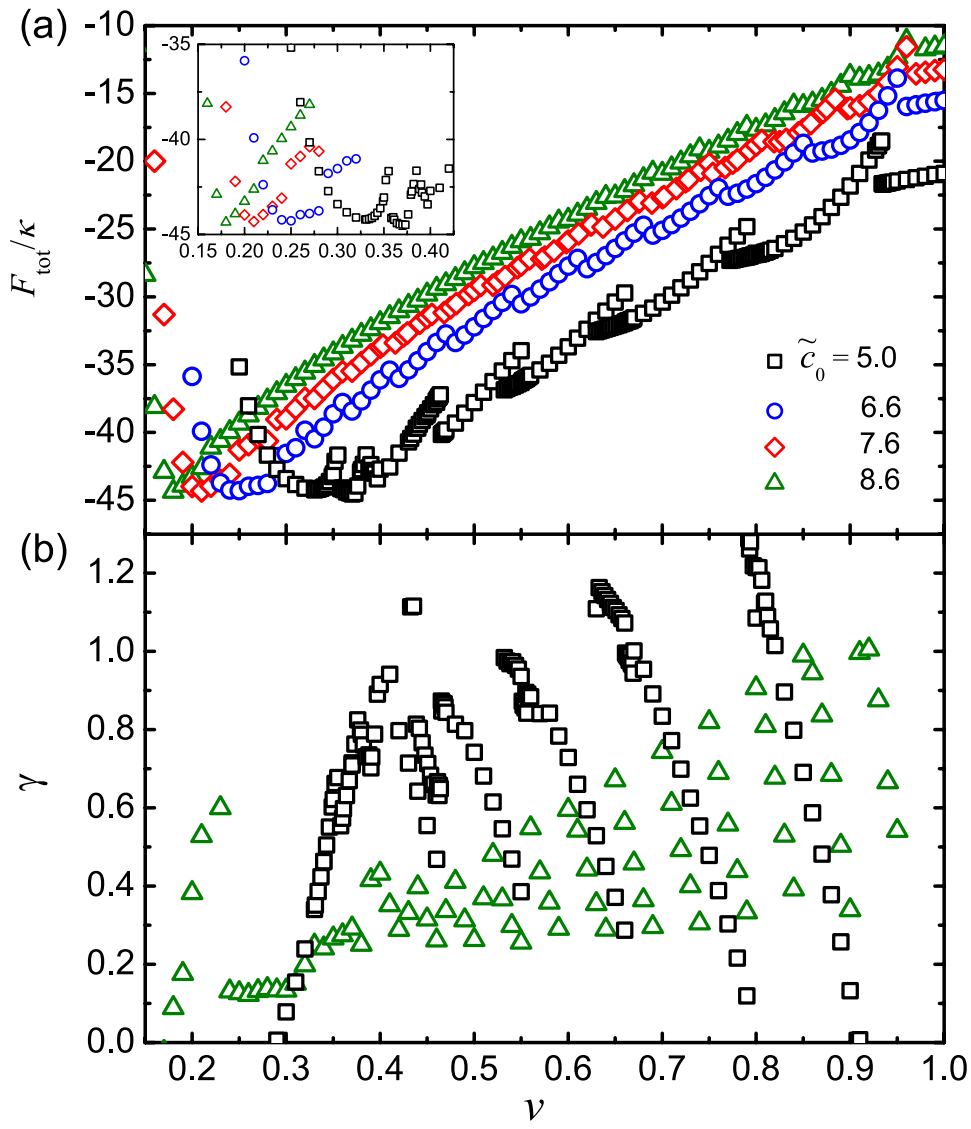

Figure 4.4: (a) The total free energy $F_{\rm tot}$ as a function of the reduced volume v with the reduced chemical potential $\tilde{\mu} = -3.56$ and various reduced spontaneous curvature $\tilde{c}_0$ values. The discontinuity of the first order derivative of $F_{\rm tot}$ occurs each time the membrane forms a new bead. Only the complete pearling states are plotted in the inset. (b) The shape parameter γ as a function of v. The symbols represent the same set of parameters as indicated in (a). The shape parameter γ jumps each time a new bead forms.

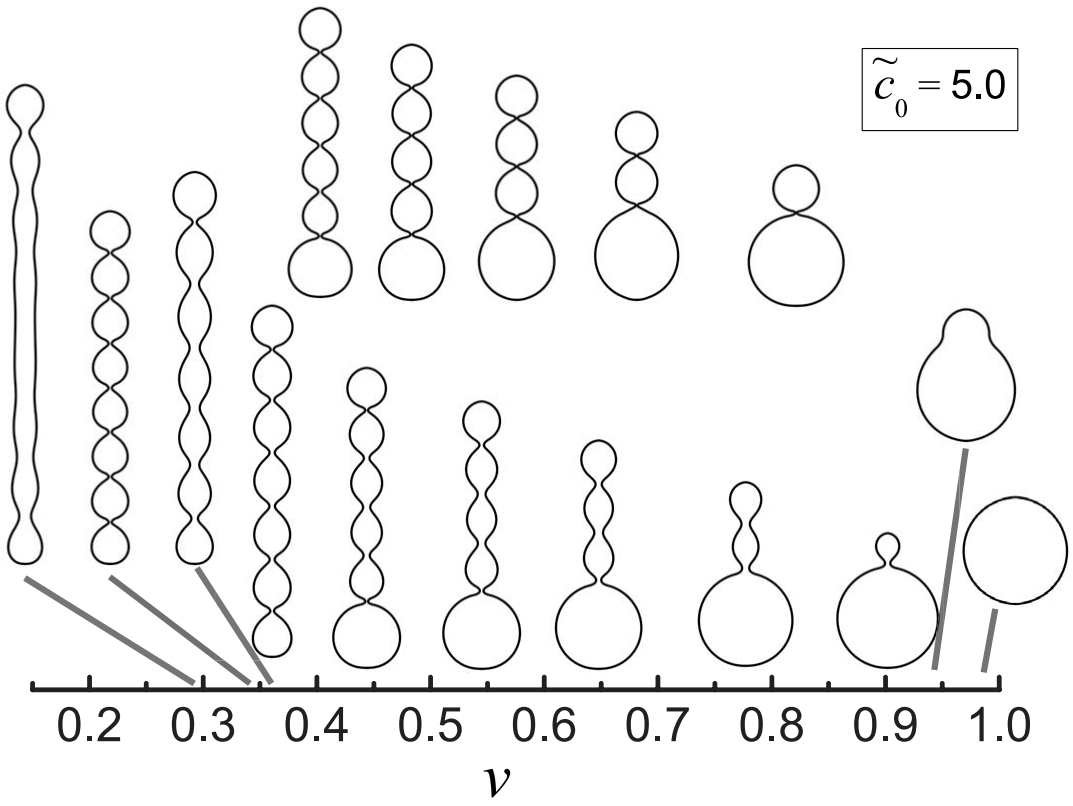

Figure 4.5: The membrane shape as a function of v for $\tilde{\mu} = -3.56$ and $\tilde{c}_0 = 5.0$.

to lower the free energy F_{tot}. The minimum of F_{tot} is achieved when the whole vesicle becomes a string of beads, which is the stable (equilibrium) state in this case. This behavior agrees with the experiment because, with proper nanoparticle concentration, the initially spherical vesicle always transformed into a string of beads in the experiment. Note that the transformation shown in Figs. 4.4 and 4.5 is not the transition path observed in the experiment because what we have here are the equilibrium states while experimentally the transformation is a dynamic process. A possible transition path is discussed in Sect. 4.4.4.

The total free energy F_{tot} in Fig. 4.4(a) and the shape parameter γ in Fig. 4.4(b) together implies that there is a discontinuous transition each time the protrusion grows one more bead. When crossing the transition point, the first derivative of F_{tot} is discontinuous, and γ drops drastically. Fig. 4.5 shows how the shapes change near the transition point. Interestingly, as shown in Figs. 4.4(a) inset and 4.5, soon after the whole vesicle becomes a string of beads ($\phi = 1$ throughout the vesicle), F_{tot} shows a similar behavior discussed in Ref. [101], which a vesicle with an uniform reduced spontaneous curvature $\tilde{c}_0 = 3.0$ goes from two beads to three beads and finally becomes a prolate (unstable). In our cases, the vesicle with an uniform $\tilde{c}_0 = 5.0$ goes from seven beads to eight beads and finally becomes a long narrow capped cylinder (unstable).

As the reduced spontaneous curvature $\tilde{c}_0$ increases, the beads appeared in the protrusion becomes smaller, and the difference in shape when lowering v becomes smaller. Thus, F_{tot} becomes smoother at higher $\tilde{c}_0$. The gaps appeared in the shape parameter γ when lowering the reduced volume v also becomes smaller, as shown in Fig. 4.4(b). To understand how $\tilde{c}_0$ affect the vesicle shape, varying $\tilde{c}_0$ while fixing the reduced chemical potential $\tilde{\mu}$ and v was examined in Fig. 4.6. Interestingly, by varying $\tilde{c}_0$ in Fig. 4.6(a), γ demonstrates a similar structure shown in Fig. 4.4(b) in a reverse manner, which implies that increasing $\tilde{c}_0$ or decreasing v has a similar effect on the shape of vesicles. In Fig. 4.6(b), we examined the reduced volume v_p of the protrusion. When $\tilde{c}_0 \lesssim 13$, v_p shows a discontinuous trend similar to a vesicle without the volume constraint [52]. The reduced volume of the mother vesicle is adjusted to accommodate v_p. However, when $\tilde{c}_0 \gtrsim 13$, v_p starts to change continuously. Since forming beads introduces discontinuity in v_p, this suggests the protrusion adopts a tubular structure, as shown by the shape in the top right of Fig. 4.3. Under the strong spontaneous curvature $\tilde{c}_0$, the protrusion tends to stay in a tubular structure. The physical meaning of the strong spontaneous curvature is that a nanoparticle can deform the membrane shape significantly, which is exactly the cases studied in Refs. [95] and [6]. Both studies observed that membrane-mediated interaction tends to aggregate adsorbed nanoparticles linearly and produce tubular membrane structures.

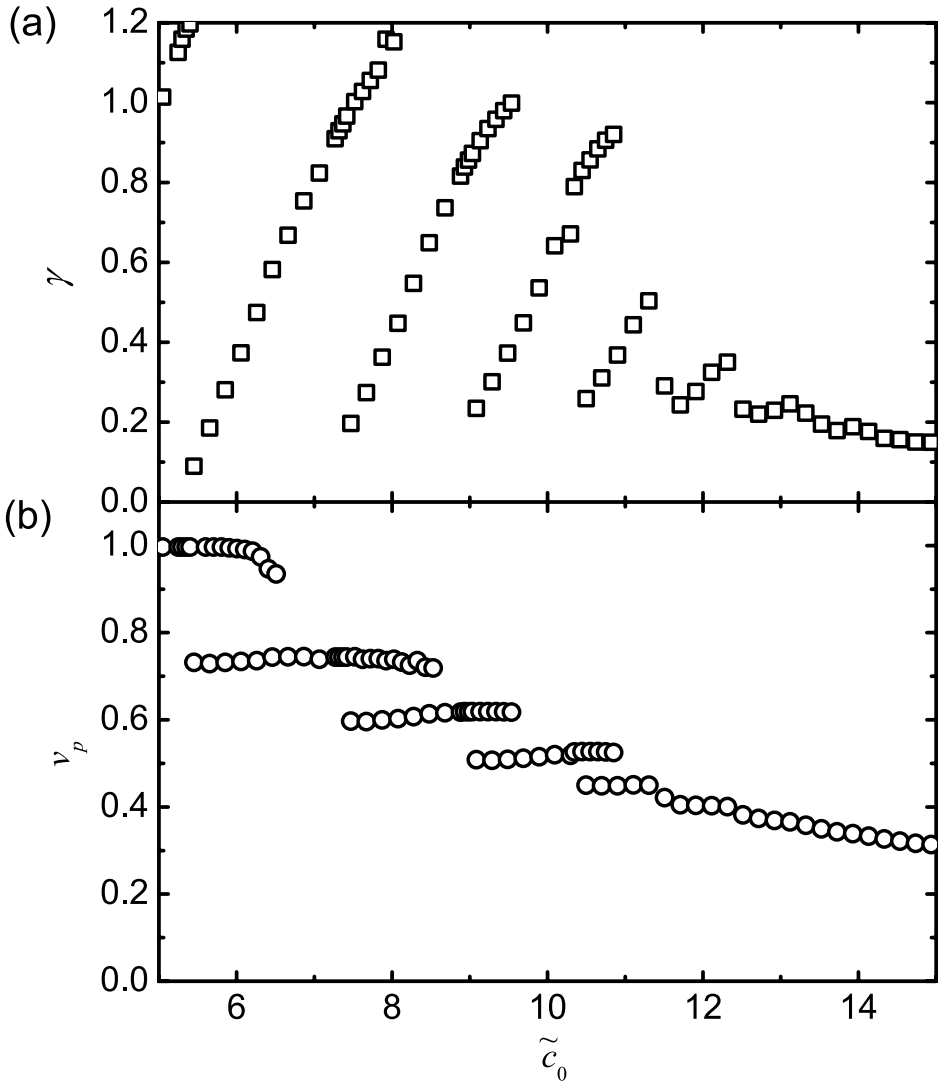

Figure 4.6: (a) The shape parameter γ as a function of the reduced spontaneous curvature $\tilde{c}_0$ for the reduced chemical potential $\tilde{\mu} = -5.1$ and reduced volume $v = 0.82$. The shape parameter γ exhibits a similar trend shown in Fig. 4.4(b) in a reverse manner. (b) The reduced volume v_p for the protrusion part decreases as $\tilde{c}_0$ increases. For $\tilde{c}_0 \lesssim 13$, the trend is similar to the one of a vesicle without the volume constraint [52].

4.4.3 Properties in $(\tilde{\mu}, v)$ plane

In a real physical system, the reduced spontaneous curvature $\tilde{c}_0$ is coupled with the adhesion strength between the vesicle surface and nanoparticles, which is also coupled with the reduced chemical potential $\tilde{\mu}$. Here we deliberately decouple $\tilde{c}_0$ and $\tilde{\mu}$ to explore the morphology transformation induced by nanoparticles with different chemical potential. A phase diagram in $(\tilde{\mu}, v)$ plane is displayed in Fig. 4.7. The apparent stripe patterns suggests that the equilibrium shapes of the vesicle is solely determined by $\tilde{c}_0$ and v with a large enough size of $\tilde{\mu}$. In weak $\tilde{\mu}$ region, when v goes smaller, the protrusion forms a tubular shape, which is similar to larger $\tilde{c}_0$ cases. Meanwhile, increasing the size of $\tilde{\mu}$ drives the membrane into a pearling shape. This is because a larger size of $\tilde{\mu}$ prompts the system to take more membrane area from the mother vesicle, which stays in a spherical shape, to form the shape according to $\tilde{c}_0$ in the protrusion. Forming spherical beads in the protrusion can accommodate the highest volume and enables more membrane area from the mother vesicle to adopt the shape according to $\tilde{c}_0$.

To understand the effect of the reduced chemical potential $\tilde{\mu}$ in more details, we studied how the shape goes from a tube to pearls in Figs. 4.8 and 4.9. First, in Fig. 4.8(a), we found that the total free energy F_{tot} is dominated by the chemical potential energy F_{ad}; however, take a closer look at the membrane energy F_{mem} in Fig. 4.8(b), the discontinuity of the first derivative of F_{mem} implies that a discontinuous transition happens at $\tilde{\mu} = -0.34$. Indeed, the shape parameter γ in Fig. 4.8(c) shows an abrupt jump which indicates a sudden change of the shape. The shapes are plotted in Fig. 4.9 that the protrusion goes from a tubular structure to a string of beads.

4.4.4 Comparing with experimental results

One important message here is that the morphology of protrusion depends on a subtle balance between the spontaneous curvature, the chemical potential, and the reduced volume. We would like to point out that the pearling process has two stages in the experiment: first, the protrusion happens and grows into tubes; second, the tubular protrusion transforms into a string of beads [119]. The first stage implies that the relaxation dynamic of the nanoparticle adhesion should be much slower than the one of the membrane reshaping. Otherwise, the pearling structure would be observed in the early stage based on our numerical results that the equilibrium shapes are pearling structures during the volume decreasing process. Next, we further argue that the growth in tubes in the experiment can be understood from Fig. 4.7 since weak $\tilde{\mu}$ implies less nanoparticles are adsorbed onto the membrane. Thus, the first stage (tubulation) corresponds to a process of decreasing

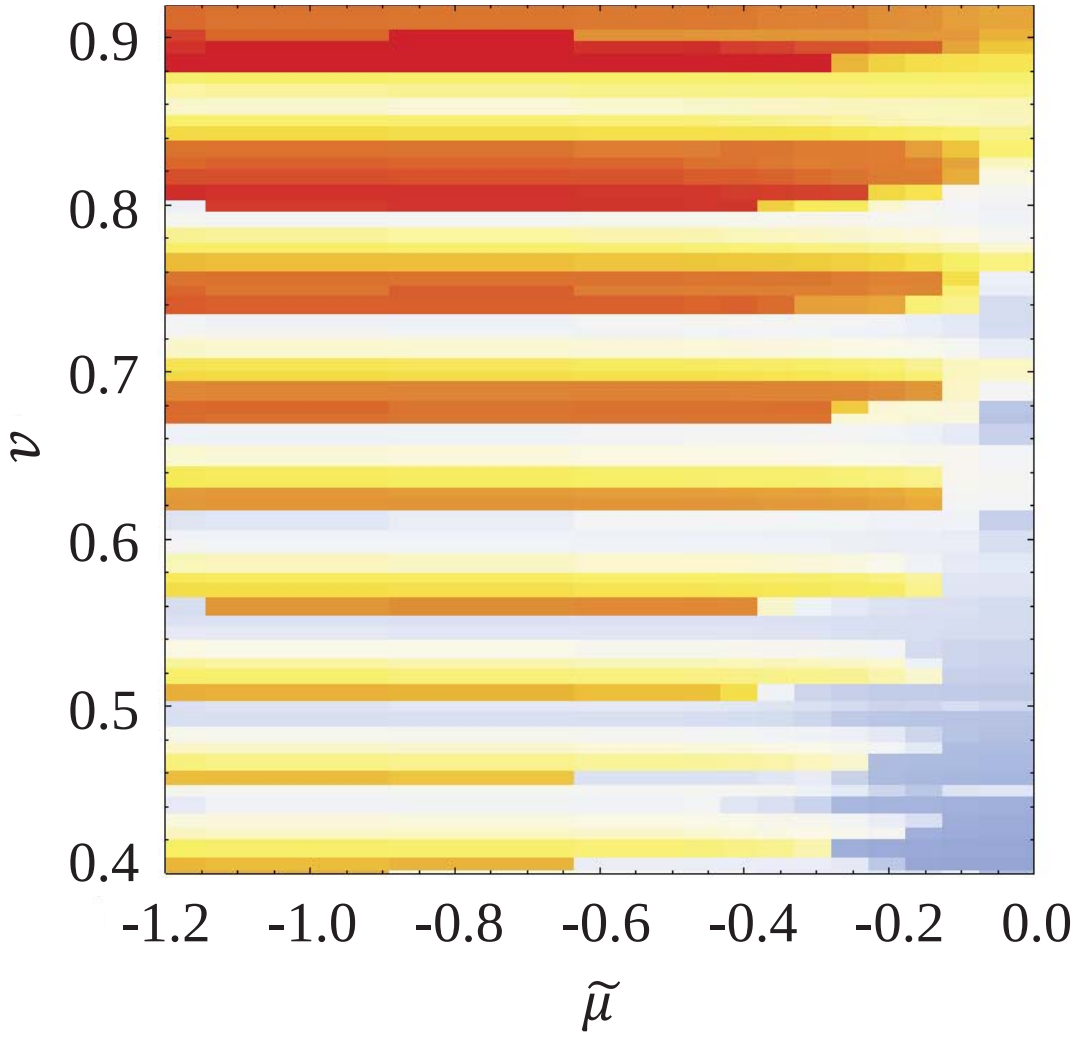

Figure 4.7: Phase diagram of the reduced volume v versus the reduced chemical potential $\tilde{\mu}$ for the reduced spontaneous curvature $\tilde{c}_0 = 7.6$. The color scheme is the same as the one in Fig. 4.3. The shapes of protrusion are affected by both v and $\tilde{\mu}$. Increasing $\tilde{\mu}$ transforms the membrane into a string of beads, while the number of beads solely depends on v and $\tilde{c}_0$.

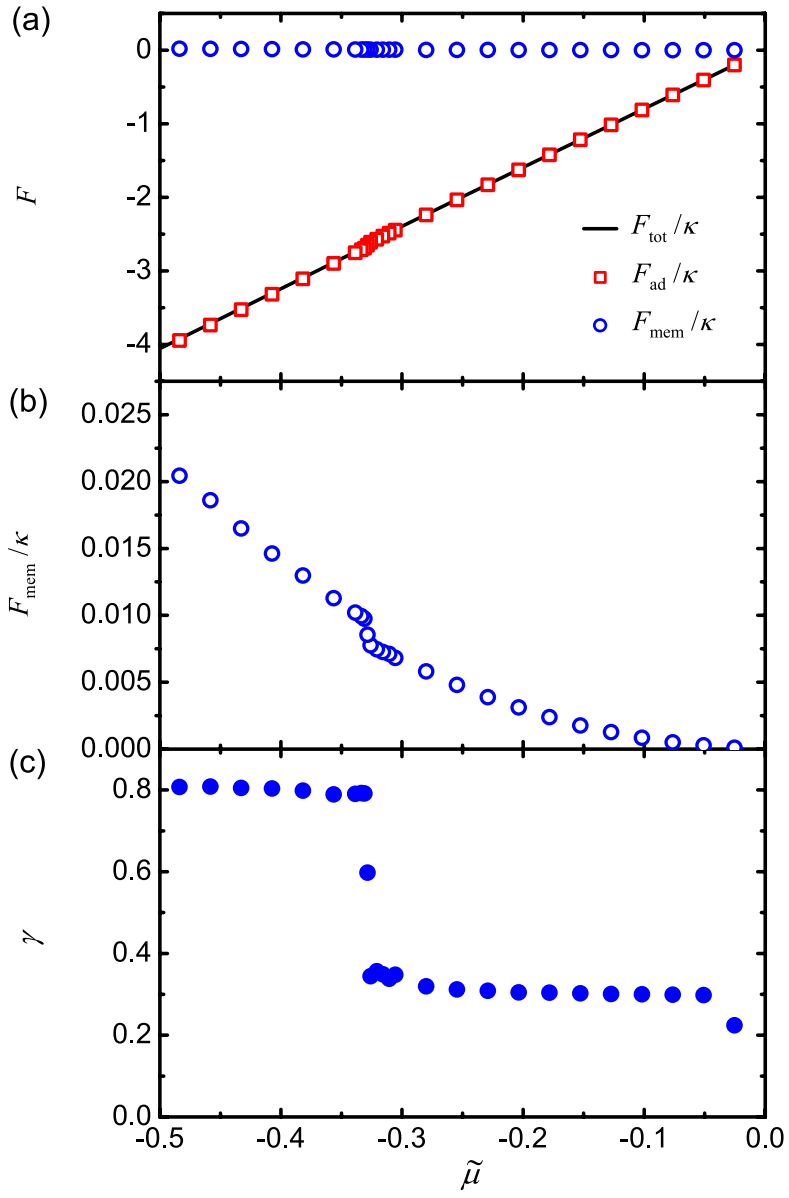

Figure 4.8: (a) The total free energy $F_{\rm tot}/\kappa$ and its components, $F_{\rm ad}$ and $F_{\rm mem}$, for the reduced spontaneous curvature $\tilde{c}_0 = 7.6$ and reduced volume $v = 0.51$. $F_{\rm tot}$ is dominated by $F_{\rm ad}$; however, the membrane component $F_{\rm mem}$ (b) indicates that the first order derivative of $F_{\rm mem}$ is discontinuous at the reduced chemical potential $\tilde{\mu} = -0.34$, and (c) the shape parameter γ exhibits a jump.

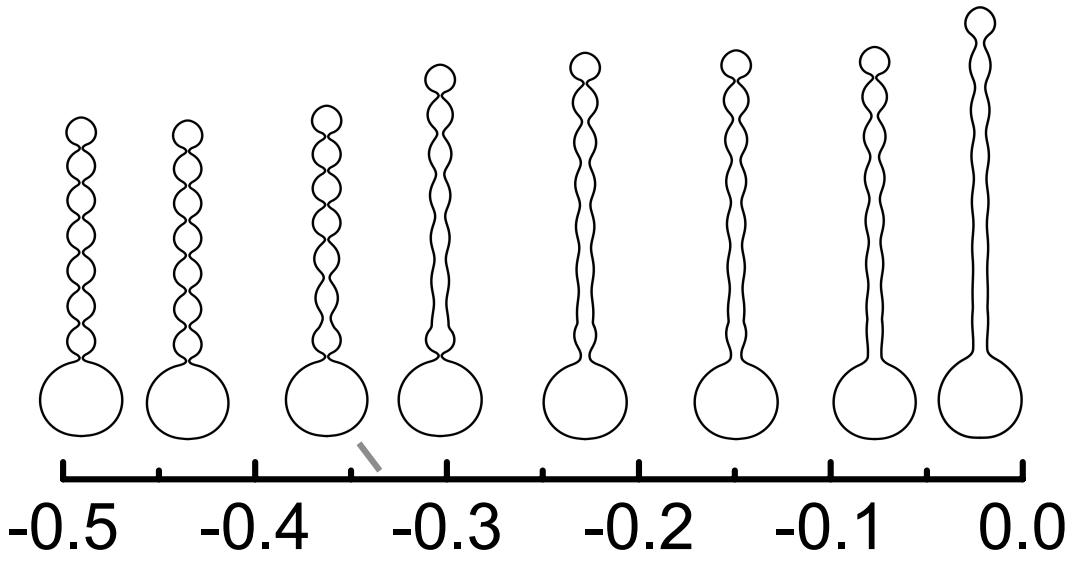

Figure 4.9: The membrane shape as a function of $\tilde{\mu}$ for $\tilde{c}_0 = 7.6$ and $v = 0.51$. The membrane forms a string of beads when $\tilde{\mu} < -0.34$.

v with a weak $\tilde{\mu}$. The reduced volume v decreases until the vesicle becomes a tubular structure. The second stage (pearling) corresponds to a process of increasing the size of $\tilde{\mu}$ as v decreases and the concentration of nanoparticles inside the vesicle increases. When the nanoparticle adhesion reaches equilibrium, which implies a large size of $\tilde{\mu}$, the vesicle turns into a string of beads, which has the lowest free energy as discussed in Fig. 4.4. The whole process is illustrated in Fig. 4.10.

4.5 Summary

In conclusion, multiple nanoparticles adsorbed onto membranes are able to induce various structures: buds, tubes, and pearls. Our results imply that the pearling structure results from a balance between the chemical potential, the deformation capability of nanoparticles, and the reduced volume of the vesicle. Details of the pearling structure is discussed. By exploring different combinations of these factors, we found the number of beads in the protrusion is mainly determined by the deformation capability of nanoparticles and the reduced volume of the vesicle. An abrupt structural transformation from a tube to pearls is found by varying the chemical potential of nanoparticles. The results are in accordance with a recent experiment and help clarify some findings in the previous studies.

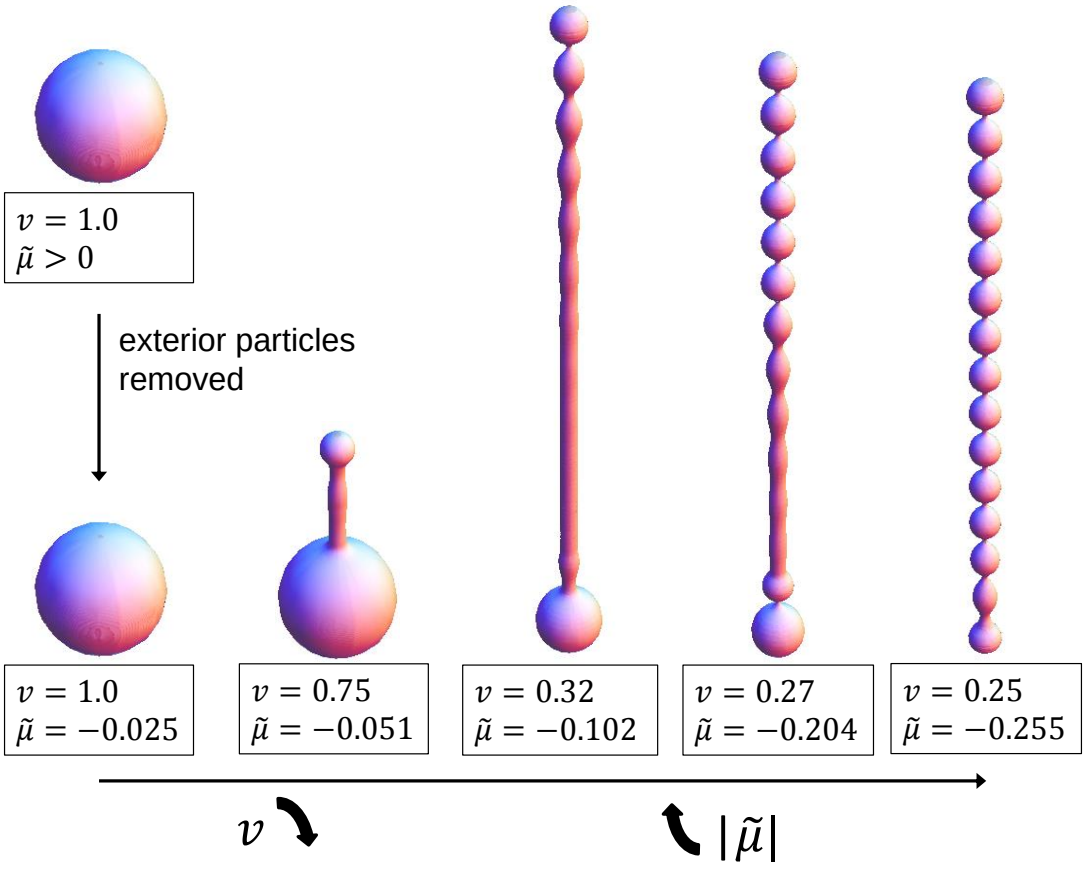

Figure 4.10: An illustration of a possible transition path. First, the volume of the vesicle decreases, and the tubular protrusion keeps growing. Next, the tube starts pearling as the size of the reduced chemical potential $\tilde{\mu}$ increases. Finally, the originally spherical vesicle turns into a long pearling shape. All the shapes are obtained from free energy minimizations for $\tilde{c}_0 = 7.6$.

Chapter 5

Conclusion and outlook

In this thesis, we studied the structures produced by interactions between macromolecules and phospholipid bilayer membranes. A large portion of previous works has focused on nanoparticles adhesion problem, which nanoparticles adheres to the membranes surface and produce different kinds of structures by deformations. Or some macromolecules, such as proteins and amphiphilic molecules, can be embedded into the layers of the membranes, creating asymmetry between the layers and hence curving the membranes. Many interesting phenomena emerge when a large number of nano-objects interact with membranes, as reviewed in Ch. 1. One important type of systems is a group of spherical nanoparticles adhering to a membrane surface. Nanoparticles move freely on the surface and generate large deformations through membrane-mediated interactions. Another type of systems is purely exploiting the excluded-volume interaction between macromolecules and membranes. By changing the mechanical properties of the membrane, macromolecules respond in dramatic structural transformations.

In Chs. 2 and 3, we showed that even though there are no active interactions between the polymer and the membrane, abrupt structural transformations still exist by changing the adhesion strength or pressure difference between the membrane and the environment. These conditions can be realized experimentally by engineering ligand-receptor bonds between the vesicle and the surface or using the micropipette to manipulate the vesicle. The adhesion case produces a balloon-like structure, yet the pressure case generates a flattened structure. The physical properties of each polymer structure are studied by computer simulations and scaling arguments, which point out that under different confining conditions the excluded-volume interaction between monomers and the confinement entropy weighs quite differently. This suggests that it is possible to experimentally study the properties of macromolecules by purely exploiting the excluded-volume interaction between polymers

and membranes. That is, the membrane itself serves as a tool provided by nature to probe the behaviors of macromolecules.

Indeed, a recent experiment conducted by Nam *et al.* utilized the excluded-volume interaction between DNAs and a bioadhesive vesicle [81]. The vesicle scrapes and staples the DNAs into frozen confinement shapes. The topology of the DNAs is then studied by optical means. Our results point out that, by controlling the adhesion and the pressure, it is possible to manipulate the polymer topology into three different forms via simple membrane interactions. In our current studies, we assumed axis symmetry for the membrane, which excludes the possibility of stretching the polymer. Thus, it is interesting to construct a truly three dimensional membrane in computer simulations to study the topology of a trapped polymer with different flexibilities. More structures and behaviors of polymers, such as self-entanglements, can be studied in the proposed model.

In Ch. 4, for nanoparticle adhering to a vesicle actively, we took a different approach based on the grand canonical ensemble [105]. Previous studies [92, 6, 95] show that the nanoparticles can generate tubular structures and buddings by membrane-mediated interaction. However, the pearling structures observed in the experiment [119] did not appear in those simulations. By taking the system to a higher coarse-graining level, we model the adsorbed nanoparticles as a density function in the context of the spontaneous curvature model. Our model successfully reproduces the pearling structure observed in the experiment. It further reveals that the shape of the vesicle depends not only on the spontaneous curvature and the adhesion strength but also the reduced volume of the vesicle. The volume of the vesicle varies slowly during the transformation, and the formation of beads along the tubular structure starting from the tip may result from the effort of maximizing the adsorption area locally.

Based on the size of nanoparticles and the bending rigidity of a membrane, the nanoparticles self-assembled into different structures on the membrane surface [120, 95]. However, for large deformations, how the nanoparticles aggregate and generate different shapes of deformations is not yet fully understood [97]. To some extent, our results presented in Ch. 4 shed some light on such a problem. We identified that the chemical potential of bringing nanoparticles onto the membrane surface drives the tubular protrusion into a string of beads, which suggests a similar effect appears if the adhesion strength increases. Nevertheless, there is no detail about the arrangement of nanoparticles on the surface in our approach. To study such a problem, a three dimensional deformable vesicle is needed. The size of the nanoparticles should be at least one or two orders of magnitude smaller than the size of the vesicle, and the number of particles should be large. It is interesting to study not only the effect of the size of nanoparticles but also the effect of the number of nanoparticles. The fluctuations of nanoparticles adsorption and movement is expected

to come into play in the system once the number of them exceeds a certain value.

Finally, most of the theoretical studies mentioned here either ignored or partially considered the membrane fluctuations. Taking the membrane fluctuations into account may not change the current theoretical results drastically because the bending rigidities of most biological membranes are large enough to regard fluctuations as a small perturbation, but it may change how nanoparticles self-assemble to different structures on the membrane surface. Therefore, it is interesting to explore the effect of membrane fluctuations on nanoparticle adhesion problems.

All the results presented in the thesis are quite exciting as they pointed out a potential way to manipulate materials at nanoscale, either using membranes to trap and reshape macromolecules or using nano-objects to generate different kinds of membrane shapes. The ability to do so could have potential application in fabricating bio-materials and the so-called *soft machines*. We hope that the results presented here can stimulate further studies.

References

[1] B. Alberts, D. Bray, K. Hopkin, A. Johnson, J. Lewis, M. Raff, K. Roberts, and P. Walter. *Essential Cell Biology*. Garland Science, New York, 4 edition, 2013.

[2] E. Atilgan and S. X. Sun. *J. Chem. Phys.*, 126:095102, 2007.

[3] T. Auth and G. Gompper. *Phys. Rev. E*, 72:031904, 2005.

[4] K. Avramova and A. Milchev. *J. Chem. Phys.*, 124:024909, 2006.

[5] G. Ayton and G. A. Voth. *Biophys. J.*, 83:3357, 2002.

[6] A. H. Bahrami, R. Lipowsky, and T. R. Weikl. *Phys. Rev. Lett.*, 109:188102, 2012.

[7] P. Ballone and M. G. Del Popolo. *Phys. Rev. E*, 73:031404, 2006.

[8] D. Boal. *Mechanics of the Cell*. Cambridge University Press, New York, 2 edition, 2011.

[9] G. Brannigan and F. L. H. Brown. *J. Chem. Phys.*, 120:1059, 2004.

[10] G. Brannigan and F. L. H. Brown. *Biophys. J.*, 90:1501, 2006.

[11] G. Brannigan, P. F. Philips, and F. L. H. Brown. *Phys. Rev. E*, 72:011915, 2005.

[12] M. Breidenich, R. R. Netz, and R. Lipowsky. *Europhys. Lett.*, 49:431, 2000.

[13] F. Brochard, P.-G. de Gennes, and P. Pfeuty. *J. Phys.*, 37:1099, 1976.

[14] F. Brochard and J. F. Lennon. *J. Phys.*, 36:1035, 1975.

[15] F. Brochard-Wyart, P.-G. de Gennes, and P. Pfeuty. *J. de Phys.*, 37(10):1099, 1976.

[16] F. Brochard-Wyart, T. Tanaka, N. Borghi, and P.-G. de Gennes. *Langmuir*, 21:4144, 2005.

[17] R. H. Byrd, P. Lu, and J. Nocedal. *SIAM J. Sci. Comput.*, 16:1190, 1995.

[18] F. Campelo and A. Hernández-Machado. *Phys. Rev. Lett.*, 99:088101, 2007.

[19] F. Campelo and A. HernándezMachado. *Phys. Rev. Lett.*, 100:158103, 2008.

[20] P. Canham. *J. Theor. Biol.*, 26:61, 1970.

[21] S. Q. Cao, G. H. Wei, and J. Z. Y. Chen. *Phys. Rev. E*, 84:050901(R), 2011.

[22] J. Z. Y. Chen. *Phys. Rev. Lett.*, 98:088302, 2007.

[23] J. Z. Y. Chen. *Phys. Rev. E*, 82:060801(R), 2010.

[24] J. Z. Y. Chen, Y. Liu, and H. J. Liang. *Phys. Rev. Lett.*, 102:168103, 2009.

[25] J. Z. Y. Chen and S. Mkrtchyan. *Phys. Rev. E*, 81:041906, 2010.

[26] M.-J. Colbert, F. Brochard-Wyart, C. Fradin, and K. Dalnoki-Veress. *Biophys. J.*, 99:3555, 2010.

[27] M.-J. Colbert, A. N. Raegen, F. Fradin, and K. Dalnoki-Veress. *Eur. Phys. J. E*, 30:117, 2009.

[28] I. R. Cooke and M. Deserno. *J. Chem. Phys.*, 123:224710, 2005.

[29] I. R. Cooke, K. Kremer, and M. Deserno. *Phys. Rev. E*, 72:011506, 2005.

[30] D. Cuvelier, N. Chiaruttini, P. Bassereau, and P. Nassoy. *Europhys. Lett.*, 71:1015, 2005.

[31] S. Das and Q. Du. *Phys. Rev. E*, 77:011907, 2008.

[32] F. David and S. Leibler. *J. de Phys. II*, 1(8):959, 1991.

[33] P. G. de Gennes. *Scaling Concepts in Polymer Physics*. Cornell University Press, Ithaca, NY, 1979.

[34] D. S. Dean, T. C. Hammant, R. R. Horgan, A. Naji, and R. Podgornik. *J. Chem. Phys.*, 137:144904, 2012.

[35] I. Derényi, F. Jülicher, and J. Prost. *Phys. Rev. Lett.*, 88(23):238101, 2002.

[36] M. Deserno. *Phys. Rev. E*, 69:031903, 2004.

[37] M. Deserno and T. Bickel. *Europhys. Lett.*, 62:767, 2003.

[38] H. Diamant. *Phys. Rev. E*, 84(6):061123, 2011.

[39] H.-G. Döbereiner, G. Gompper, C. K. Haluska, D. M. Kroll, P. G. Petrov, and K. A. Riske. *Phys. Rev. Lett.*, 91:048301, 2003.

[40] T. Dotera and Y. Y. Suzuki. *Phys. Rev. E*, 62:5318, 2000.

[41] J. M. Drouffe, A. C. Maggs, and S. Liebler. *Science*, 254:1353, 1991.

[42] H. Ewers *et al. Nat. Cell Biol.*, 12:11, 2010.

[43] E. Evans, H. Bowman, A. Leung, D. Needham, and D. Tirrell. *Sience*, 273:933, 1996.

[44] O. Farago. *J. Chem. Phys.*, 119:596, 2003.

[45] O. Farago. *Phys. Rev. E*, 84(5):051914, 2011.

[46] J. F. Faucon, M. D. Mitov, and P. Bothorel.

[47] J. R. Frank and M. Kardar. *Phys. Rev. E*, 77(4):041705, 2008.

[48] H. Gao, W. Shi, and L. B. Freund. *Proc. Natl. Acad. Sci. USA*, 102:9469, 2005.

[49] R. Goetz, G. Gompper, and R. Lipowsky. *Phys. Rev. Lett.*, 82:221, 1999.

[50] R. Goetz and R. Lipowsky. *J. Chem. Phys.*, 108:7397, 1998.

[51] G. Gompper and D. M. Kroll. *J. Phys.: Condens. Matter*, 9:8795, 1997.

[52] W. T. Góźdź. *Langmuir*, 20:7385, 2004.

[53] W. T. Gozdz. *Langmuir*, 25:5665, 2007.

[54] A. Halperin, P. Pincus, and S. Alexander. *J. de Phys. Lett.*, 46(12):543, 1985.

[55] W. Helfrich. *Z. Natureforsch. C*, 28:693, 1973.

[56] J. Henriksen, A. C. Rowat, and J. H. Ipsen. *Eur. Biophys. J.*, 33:732, 2004.

[57] M.-L. Hisette, P. Haddad, T. Gisler, C. M. Marques, and A. P. Schröder. *Soft Matter*, 4:828, 2008.

[58] M. Hu, J. J. Briguglio, and M. Deserno. *Biophys. J.*, 102(6):1403, 2012.

[59] J. N. Israelachvili, D. J. Mitchell, and B. W. Ninham. *J. Chem. Soc., Faraday Trans. 2*, 72:1525, 1976.

[60] H. Jiang and T. R. Powers. *Phys. Rev. Lett.*, 101:018103, 2008.

[61] W. Jiang, B. Y. Kim, J. T. Rutka, and W. C. Chan. *Nat. Nanotechnol.*, 3:145, 2008.

[62] Y. W. Kim and W. Sung. *Phys. Rev. E*, 63:041910, 2001.

[63] T. Kohyama. *Physica A*, 388:3334, 2009.

[64] I. Koltover, J. O. Rädler, and C. R. Safinya. *Phys. Rev. Lett.*, 82:1991, 1999.

[65] E. Kreyszig. *Differential Geometry*. Dover, New York, 1991.

[66] H. Kusumaatmaja and R. Lipowsky. *Soft Matter*, 7:6914, 2011.

[67] M. Laradji and P. B. Sunil Kumar. *Phys. Rev. Lett.*, 93:198105, 2004.

[68] Y. Li and N. Gu. *J. Phys. Chem. B*, 114:2749, 2010.

[69] Y. Li, H. Miao, H. Ma, and J. Z. Y. Chen. *Soft Matter*, 9:11461, 2013.

[70] E. Lindahl and O. Edholm. *Biophys. J.*, 79:426, 2000.

[71] R. Lipowsky and H. G. Döbereiner. *Europhys. Lett.*, 43:219, 1998.

[72] R. Lipowsky, H.-G. Döbereiner, C. Hiergeist, and V. Indrani. *Physica A*, 249:536, 1998.

[73] M. S. Long, A. S. Cans, and C. D. Keating. *J. Am. Chem. Soc.*, 130:756, 2008.

[74] S. J. Marrink, A. H. de Vries, and A. E. Mark. *J. Phys. Chem. B*, 108:750, 2004.

[75] S. J. Marrink, H. J. Risselada, S. Yefimov, D. P. Tieleman, and A. H. de Vries. *J. Phys. Chem. B*, 111:7812, 2007.

[76] L. Miao, U. Seifert, M. Wortis, and H.-G. Döbereiner. *Phys. Rev. E*, 49:5389, 1994.

[77] S. Mkrtchyan, C. Ing, and J. Z. Y. Chen. *Phys. Rev. E*, 81:011904, 2010.

[78] M. Müller, K. Katsov, and M. Schick. *Physics Reports*, 434:113, 2006.

[79] M. M. Müller, M. Deserno., and J. Guven. *Europhys. Lett.*, 69:482, 2005.

[80] M. M. Müller, M. Deserno, and J. Guven. *Phys. Rev. E*, 76:011921, 2007.

[81] G. Nam, M. L. Hisette, Y. L. Sun, T. Gisler, A. Johner, F. Thalmann, A. Schröder, C. M. Marques, and N.-K. Lee. *Phys. Rev. Lett.*, 105:088101, 2010.

[82] H. Noguchi and G. Gompper. *Proc. Natl. Acad. Sci. USA*, 102:14159, 2005.

[83] H. Noguchi and M. Takasu. *Phys. Rev. E*, 64:041913, 2001.

[84] H. Noguchi and M. Takasu. *Biophys. J.*, 83:299, 2002.

[85] R. K. Pathria and Paul D. Beale. *Statistical Mechanics*. Butterworth-Heinemann, Burlington, MA, 3 edition, 2011.

[86] S. Pierrat, F. Brochard-Wyart, and P. Nassoy. *Biophys. J.*, 87:2855, 2004.

[87] R. Podgornik. *Europhys. Lett.*, 21:245, 1993.

[88] D. Raucher and M. P. Sheetz. *Biophys. J.*, 38:29, 1982.

[89] W. Reisner, K. J. Morton, R. Riehn, Y. M. Wang, Z. Yu, M. Rosen, J. C. Sturm, S. Y. Chou, E. Frey, and R. H. Austin. *Phys. Rev. Lett.*, 94:196101, 2005.

[90] J. D. Revalee, M. Laradji, and P. B. Sunil Kumar. *J. Chem. Phys.*, 128:035102, 2008.

[91] B. J. Reynwar and M. Deserno. *Soft Matter*, 7:8567, 2011.

[92] B. J. Reynwar, G. Illya, V. A. Harmandaris, M. M. Müller, K. Kremer, and M. Deserno. *Nature*, 447:461, 2007.

[93] Y. Roiter, M. Ornatska, A. R. Rammohan, J. Balakrishnan, D. R. Heine, and S. Minko. *Nano Lett.*, 8:941, 2008.

[94] T. Roopa and G. V. Shivashankar. *Appl. Phys. Lett.*, 82:1631, 2003.

[95] A. šarić and A. Cacciuto. *Phys. Rev. Lett.*, 108:118101, 2012.

[96] A. šarić and A. Cacciuto. *Phys. Rev. Lett.*, 109:188101, 2012.

[97] A. šarić and A. Cacciuto. *Soft Matter*, 9:6677, 2013.

[98] M. B. Schneider, J. T. Jenkins, and W. W. Webb. *Biophys. J.*, 45:891, 1984.

[99] M. B. Schneider, J. T. Jenkins, and W. W. Webb. *Biophys. J.*, 45:1457, 1984.

[100] U. Seifert. *Advances in Physics*, 46:13, 1997.

[101] U. Seifert, K. Berndl, and R. Lipowsky. *Phys. Rev. A*, 44:1182, 1991.

[102] U. Seifert and R. Lipowsky. *Phys. Rev. A*, 42:4768, 1990.

[103] K. A. Smith, D. Jasnow, and A. C. Balazs. *J. Chem. Phys.*, 127:084703, 2007.

[104] J. C. Stachowiak, C. C. Hayden, and D. Y. Sasaki. *Proc. Natl. Acad. Sci. USA*, 107:7781, 2010.

[105] Y.-C. Su and J. Z. Y. Chen. *in preparation.*

[106] Y.-C. Su and J. Z. Y. Chen. *Soft Matter*, 9:570, 2013.

[107] Y.-C. Su and J. Z. Y. Chen. *Phys. Rev. E*, 87:052706, 2013.

[108] F. Thalman, V. Billot, and C. M. Marques. *Phys. Rev. E*, 83:061922, 2011.

[109] M. Tokarz, B. Akerman, J. Olofsson, Jean-Francois Joanny, Paul Dommersnes, and O. Orwar. *Proc. Natl. Acad. Sci. USA*, 102:9127, 2005.

[110] I. Tsafrir, Y. Caspi, M.-A. Guedeau-Boudeville, T. Arzi, and J. Stavans. *Phys. Rev. Lett.*, 91:138102, 2003.

[111] I. Tsafrir, D. Sagi, T. Arzi, M.-A. Guedeau-Boudeville, V. Frette, D. Kandel, and J. Stavans. *Phys. Rev. Lett.*, 86:1138, 2001.

[112] R. Vácha, F. J. Martinez-Veracoechea, and D. Frenkel. *Nano Lett.*, 11:5391, 2011.

[113] Z.-J. Wang and M. Deserno. *J. Phys. Chem. B*, 114:11207, 2010.

[114] Z.-J. Wang and D. Frenkel. *J. Chem. Phys.*, 122:234711, 2005.

[115] T. R. Weikl. *Eur. Phys. J. E*, 12:265, 2003.

[116] S. Yamamoto and S. Hyodo. *J. Chem. Phys.*, 118:7937, 2003.

[117] K. Yang and Y. Ma. *Aust. J. Chem.*, 64:894, 2011.

[118] X. Yi, X. Shi, and H. Gao. *Phys. Rev. Lett.*, 107:098101, 2011.

[119] Y. Yu and S. Granick. *J. Am. Chem. Soc.*, 131:14158, 2009.

[120] T. Yue and X. Zhang. *ACS Nano*, 6:3196, 2012.